UiT
THE ARCTIC
UNIVERSITY
OF NORWAY

Department of Physics and Technology – Faculty of Science and Technology

Charging Effects and Detection of Mesospheric Dust with the Instrument SPID on the G-Chaser Rocket

—

Tinna LÍf Gunnarsdóttir

FYS-3931 Master thesis in Space Physics, June 2019

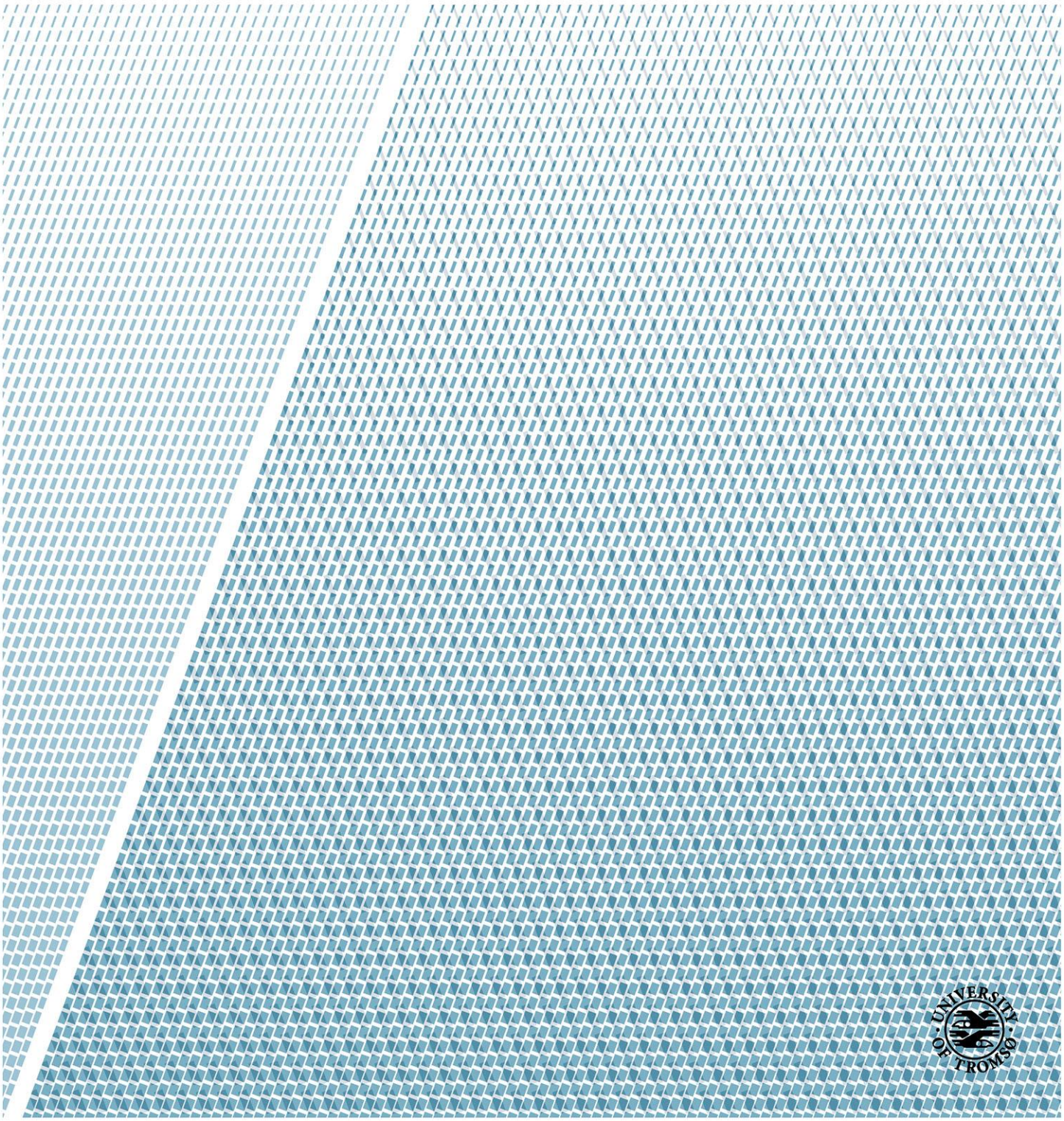

Abstract

Smoke Particle Impact Detector (SPID) is a faraday cup impact probe designed and built by the University of Tromsø(UIT). Its main purpose is to measure nanometer sized smoke particles (in-situ) in the atmosphere, and to do that it needs to be launched on a sounding rocket. Its design is an open faraday cup with grids to shield out ambient plasma and a larger slanted impact grid to measure the incoming smoke. The particles we are interested in measuring are called Meteoric Smoke Particles (MSPs). They are believed to be condensed material from meteoric ablation and thought to reside in layers in the altitude range of approximately 50-100 km with sizes of around 0.2-3 nm on average. There are many unknowns regarding the smoke particles, particularly their altitude distribution, size, charge and composition. By gaining more knowledge about them we can start to understand better their involvement in atmospheric processes including their possible impact on chemical reactions and formation of ice particles in the mesosphere and the possible connection to Polar Mesospheric Winter Echoes(PMWE). SPID was launched for the first time on the student rocket G-Chaser in January 2019. The launch was successful apart from some minor issues regarding amplification on the shielding grids. The main grid designed to measure the smoke showed a positive current during the entire flight with some interesting areas that might indicate detection of smoke particles. This thesis focuses on estimating the charging of the payload by ambient plasma and induced photocurrent from UV solar photons, as well as the possibility of solar induced currents on the grids and their possible contribution to the measured currents. We find that the payload is primarily negatively charged with an estimated floating potential of maximum 0.46 V up towards apogee of around 184 km with charging due to ambient electrons dominating the examined charging sources. Calculations also determined that there it is possible for the induced photocurrent on the grids to be the cause of the magnitude difference seen in the measured signals due to the spin of the rocket and its coning motion. Another part of the thesis is to examine and determine the charging of the smoke inside the probe, to compare the measured current to theoretical values and examine the various error factors associated with this. Based on theoretical considerations it was explored how the work function of the particles, the depen-

dence of particle properties, their size as well as their initial velocity depended on the their ability to generate charge. Investigations carried out within this thesis showed that there are considerable differences between available charging models, as well as altitude distribution discrepancies between the models and the measured probe current. Possible causes of discrepancies can be due to models used are from and Further investigation is needed to determine the accurate altitude distribution of smoke particles. Since the distribution model we used is from a different time of year, this might explain the possible difference. We conclude the charging mechanism as the grains collide with the measuring plate are not well defined, a task for future dedicated laboratory experiments to describe how small grains of nanometer size can gain charge in these kind of collisions. Which would help to better define and choose an accurate charging model for very small particles in such high velocity collisions.

Acknowledgements

Thanks to my supervisor Ingrid Mann for her dedicated assistance, patience and help, to my partner in crime Henriette Trollvik for invaluable help and input, Tarjei Antonsen and Ove Havnes for their discussions and contributions. Special thanks to the SPID G-Chaser project leader shild Fredriksen for giving me and the other students the opportunity to work on a rocket mission and be apart of the design process of SPID.
Many thanks to the entire SPID team especially Sveinung Olsen and Yngve Eilertsen for their dedication and help and all the fun. Thanks to my office pals and master-student buddies and the Space Physics group as a whole.
And a "thousand thank yous" to Knut Erik and Emma and my entire family, you are an inspiration every last one of you and I am so lucky to have you in my life. You are so amazing and supportive and I could not have done this without you!

Contents

1 Introduction **15**

2 Meteoric Smoke Particles **17**
2.1 Earth's Atmosphere 17
2.1.1 Mesosphere 19
2.1.2 Meteor Ablation 20

3 Background **23**
3.1 G-Chaser 23
3.2 Smoke Particle Impact Detector - SPID 24
3.2.1 SPID heritage: DUSTY and MUDD 24
3.2.2 SPID Design 25

4 Payload Charging **31**
4.1 Charging due to Ambient Plasma 31
4.2 Photoemission/Photocurrent 32
4.2.1 The Solar Spectrum 32
4.2.2 Atmospheric Absorption and Optical Depth 34
4.2.3 Solar Zenith Angle 37

5 Collisional Dust Charging **41**
5.1 Triboelectric Charging 41
5.2 Charging Models 43
5.2.1 Adams & Smith - 1970 43
5.2.2 Walter John - 1995 44
5.2.3 Matsusaka et al. - 2010 44
5.2.4 Wang & John - 1988 45
5.3 Charge Limit 46

6 Flight and Measurement Data **49**
6.1 SPID Measurements 54

7 Payload Charging - Results **59**
7.0.1 Solar Zenith Angle 59
7.0.2 Payload Charging due to photoemission 60
7.0.3 Charging due to ambient plasma 69
7.0.4 Total charge on payload section 73

8 Charge of Particles inside the probe - results **79**
8.1 Maximum Charge on Nanoparticles 81
8.2 Charging Models 82
8.3 Varying Model Parameters 85
8.3.1 Work Function Dependence 85
8.3.2 Particle Density Dependance 87
8.3.3 Separation Distance Dependence 88
8.4 Particle Speed Dependance 90
8.5 Resulting Current 91

9 Conclusion and Discussion **99**

List of Figures

2.1 Earths different atmospheric layers, atmospheric neutral temperature, neutral number density. Both neutral temperature and neutral density are from the NRLMSISE-00 atmospheric model at time of the G-Chaser launch. Special thanks to Dr. Lutz Rastaetter for providing access to the data (CCMC, Accessed: 2019-05-28) 18
2.2 Temperature at 87 km altitude for all altitudes and all months of the year. Figure from Plane et al. (2015) - output from WACCM . 19
2.3 Number densities for 11 size bins with radius ranging from 0.2-22 nm, of positive, negative and neutral smoke particles. Plotted from data provided by Baumann et al. (2015), based on a model by Megner et al. (2006). 21
2.4 Comparison of the concentration of MSPs between winter (DJF) and summer (JJA) with focus on the dashed line representing ¿60°N which should resemble the conditions of the rocket launch at latitude above 69 °N. Figure from Bardeen et al. (2008)(Open Access) . . . 21

3.1 Payload section of the rocket. SPID marked with UIT location in the top deck along with PARM the Japanese team. Teams VT and WVU did not end up flying on the rocket. Figure: Chris Koehler, Colorado Space Grant Consortium 24
3.2 SPID heritage instruments MUDD and DUSTY a) DUSTY probe (Havnes et al., 1996) b) MUDD probe (Antonsen et al., 2017) . . . 25
3.3 SPID probe 3D drawing and outside dimensions. Drawing from Solidworks by UIT/Sveinung Olsen 26
3.4 Cross section of SPID with dimensions between the grids inside the probe. Drawing in Solidworks by Sveinung Olsen 27
3.5 Middle plate and silver coated brass grids prior to assembly. Figure: Sveinung Olsen 28
3.6 Image of SPID and PARM on the top deck, at Andoya Space Center for final integration and testing prior to launch- Figure: NASA/Wallops Flight Facility 29

4.1 Reference solar irradiance spectrum per wavelength in nanometers above earths atmosphere (often called AM0). Marked in red is the UV portion fo the solar spectrum. Plotted with data from (NREL, Accessed: 2019-05-22) 33
4.2 Ratio of solar spectrum measured on 19 of February 1979 to 10 of July 1976, the latter observation was at a very low solar activity with almost no sunspots visible on the suns surface. Reprinted from Planetary and Space Science,Vol 31/Issue 6, R.G Roble and B.A Emery, On the global mean temperature of the thermosphere, Pages 597-614., Copyright (1983), with permission from Elsevier.(Hinteregger, 1981; Roble and Emery, 1983) 34
4.3 Geometry for calculating the optical depth,χ_0, at the location of the rocket launch. Not to scale. We are Interested in when the solar zenith angle is $\chi_0 > 90$. Reprinted from Physics and Chemistry of the Upper Atmosphere, M. H. Rees, Copyright (1989), with permission of Cambridge University Press through PLSclear. 36

5.1 Showing the main mechanisms behind metal to metal contact for metals with different work functions. (Matsusaka et al., 2002, 2010) Reprinted from Chemical Engineering Science,Vol 65/Issue 22, S.Matsusakaa, H.Maruyamaa, T.Matsuyama and M.Ghadiric, Triboelectric charging of powders: A review, Pages 5781-5807, Copyright (2010), with permission from Elsevier. 42

6.1 On the left is shown the altitude of the rocket with time of flight for the rocket, showing in dashed lines the maximum altitude, with apogee of around 184 km.On the right is the latitude and longitude of the rocket from the GPS measurements from the telemetry measurement section of the rocket, with the launch point being the lowest point of the graph at 69 degrees north and 16 degrees east. The data used to plot the figure is provided by NASA Wallops Flight Facility 50
6.2 Figure part a) shows the altitude of the rocket plotted with the total velocity with the dashed line marking the apogee as before. The small dot-dashed lines on the left indicate the end for the first and second stage burnouts. of the rocket. Figure part b) shows the total velocity vector compared to the velocity vectors in x, z, and y direction. The data used to plot the figures is provided by NASA Wallops Flight Facility 51

6.3 Comparison of the acceleration vectors, z, x and y direction. Plot of all the acceleration vectors, z, x and y direction. Marked in red is the end of first burnout, start end end of the seconds burnout, the apogee and when the rocket starts to encounter atmosphere. The data used to plot the figures is provided by NASA Wallops Flight Facility 52
6.4 Plot fo the power measurements to the instrument section. SPID shares this section with the JAXA/PARM team, their instruemnt had a power ramp up at 62 seconds that is shown in the plot. The data used to plot the figures is provided by NASA Wallops Flight Facility 53
6.5 Plot of the measurements by the magnetometers on the rocket. Showing the de-spin and nosecone ejection Data from NASA Wallops/Santiago 54
6.6 Overview of the collected data from all of the grids with time. The top grids can be seen to be saturated soon after the nosecone is ejected. 55
6.7 Overview of the collected data from the three bottom grids with time. From ejection of the nosecone to atmospheric reentry. 56
6.8 Measured current by the middle plate on the up-leg and down-leg of the rocket 57

7.1 Solar Irradiance in the UV part of the spectrum (115-300 nm). Top figure showing the entire UV part of the spectrum, middle part shows the range 115-180 nm, where the sharp peak at 121 nm is the Lyman alpha line - marked in red. The bottom image is the 180-300 nm range. Data from (of Colorado Boulder, Accessed: 2019-04-01) 61
7.2 Mean values of the Ozone number density for the entire data from the Ozone database and the comparison of the average values (Bodeker et al., 2013) 62
7.3 Number density and absorption cross section of molecular oxygen and ozone for altitudes 0-200 km and wavelengths of 115-300 nm. The absorption cross section of molecular oxygen is only taken up to 189. 63
7.4 Note: axis not the same 64
7.5 Number of photons generated per wavelength for selected altitudes of 80, 90, 120, 150 and 180 km. There are virtually no photons created below 75 km altitude due to the high solar zenith angle and large amount of atmosphere the irradiance has to go through 65

7.6 Material properties for the metals that are considered; the photoelectric yield and the reflectance for the wavelength ranges of 115 to 300 nm(Giono et al., 2018) 66
7.7 The estimated photocurrent for an aluminium cylinder at altitudes 70 to 180 km are shown. The current below 70 km is so small it is essentially zero. Possible photocurrent with a maximum current of about 0.45 mA 67
7.8 Comparison of the measured signal from the middle plate to the possible photocurrent generated for different magnitudes in direct sun. With 100 % the plate is always in the sun 68
7.9 Comparison of the measured signal from the negatively biased (-10V) GB1 grid at the bottom of the probe to the possible photocurrent generated for different magnitudes in direct sun. With 100 % the plate is always in the sun 69
7.10 Altitude of the rocket with different layers of the ionopshere 70
7.11 Measurements from the VHF EISCAT radar taken at the time of launch. With Electron density and electron and ion temperature averages. The dashed yellow line for both temperatures is used in estimations of the current contributions.Time used for the generation of the plot is from 9:13-9:18 UTC 71
7.12 Electron Thermal Velocity compared to the rocket velocity set as 1500 m/s. 72
7.13 Estimate of the payload potential, electron and ion currents with altitude. Calculations form equations 4.2, 4.4 73
7.14 Comparison of the calculated total current to the payload, with the electron current on the left, the ion current in the middle and the photocurrent on the right 74
7.15 Comparison the payload charge, possible ion current inside the probe and the ion current in the ram direction. 75
7.16 Comparison the payload charge, possible ion current inside the probe and the ion current in the ram direction. 77
7.17 Current measured on the middle plate compared to the possible current due to ions and the difference between these two currents . 78

8.1 Number Density of electrons, ions and MSPs from altitudes of 60 to 150 km. Data from model by (Megner et al., 2006) and prepared by (Baumann et al., 2015) 80
8.2 Charge limit for small particles, taking into account electron emission and disintegration of particles 82

8.3 Comparison of charging models from Adams and Smith (1971), John (1995) , Matsusaka et al. (2010) and Wang and John (1988). The number of charges, e, are plotted for each respecting charging model per particle size. The bias on the middle plate is set to zero. The dot-dashed line indicated the electron emission limit and the black dashed line represents one electron charge. 84
8.4 Comparison of charging models from Adams and Smith (1971), John (1995) , Matsusaka et al. (2010) and Wang and John (1988).The number of charges, e, are plotted for each respecting charging model per particle size. The bias on the middle plate is set to -2 V as on SPID. 85
8.5 Number of charges produced per particle radius for different metal particles with no bias on the middle plate. Using charging model by John (1995).The black dashed line represent one electron charge limit and the red dot-dashed line represents the electron emission limit. 86
8.6 Number of charges produced per particle radius for different metal particles with -2 V bias on the middle plate. Using charging model by John (1995).The black dashed lines represent 1 and 2 electron charge limit and the red dot-dashed line represents the electron emission limit. 87
8.7 Comparison of charge produced per particle size with density of 2 g/cm3 and 3g/cm3 and a -2 V biased middle plate and no bias on the middle plate.The black dot-dashed line is the electron emission limit. The particles are iron particles using the charging model of John (1995) 88
8.8 Varying the separation distance Z with multiples of the Bohr radius, between the particle and the middle plate. Using the charging model of John (1995) with a biased middle plate of -2V 89
8.9 Varying the initial impact speed of the particles as they collide with a -2 V biased middle plate. The velocity is varied from 250 to 1000 m/s. Using charging model of John (1995) 91
8.10 Total current for all size distributions for neutral MSP particles with altitude. Using data from model by Baumann et al. (2015) and Megner et al. (2006) 93
8.11 Total current for all size distributions for positive MSP particles with altitude. Using data from model by Baumann et al. (2015) and Megner et al. (2006) 93

8.12 Total current for all size distributions for negative MSP particles with altitude. Using data from model by Baumann et al. (2015) and Megner et al. (2006) 94
8.13 Comparison of the measured current from the middle plate to the calculated current from the different charging models due to neutral and positively charged particles. 95
8.14 Comparison of the measured current from the middle plate to the calculated current from the cahrging model of Wang and John (1988) by varying the particle size 96
8.15 Comparison of the measured current from GB1 grid and the charging models due to positive and neutral particles. 97
8.16 Comparison of the measured current from GB2 grid and the charging models due to negative particles. 98

Chapter 1

Introduction

Meteoric smoke particles (MSPs) are nanometer sized dust particles that reside in the Earth's atmosphere at altitudes of around 50 - 100 km. This is the upper region of the mesosphere, the layer of the atmosphere where temperature decreases with height and reaches its minimum at the mesopause. The temperature is influenced by a number of factors including atmospheric composition, circulation and waves; it is highly variable at the polar mesopause where it reaches an annual minimum during summer. Several tons of dust and meteoroids from interplanetary space enter the atmosphere per day and a large fraction of their mass ablates at altitudes around 70 - 110 km. This ablated material is thought to re-condense into meteoric smoke (Antonsen et al., 2017). It is important to study these particles and gain more knowledge about their composition, size and charge, as well as their part in atmospheric processes. They are thought to play a role in phenomena like noctilucent clouds (NLC), polar mesospheric summer echoes (PMSE) and possibly also polar mesospheric winter echoes (PMWE) (Havnes et al., 2014). The MSP's influence the charge balance in the mesosphere (Baumann et al., 2013) and when they reach the stratosphere which is the layer below the mesosphere, they can also have an influence on weather, and stratospheric phenomena (Giono et al., 2018). The small sizes and high altitude of the smoke particles make them hard to study with remote sensing devices. Little information has been gained by radar and lidar, and satellite devices have only been able to study the smoke when encased in ice in the cold summer polar mesosphere (Hervig et al., 2017). This makes rockets a good method to measure them in-situ with good height resolution. The University of Troms (UiT) has developed an instrument that is designed to measure small dust particles on a rocket payload; called the Smoke Particle Impact Detector (SPID). The probe is based on design heritage from the rocket probes DUSTY and MUDD(Multiple Dust Detector), also designed and built by UiT. These probes were focused on measuring the smoke particles in the mesosphere during the summer when the particles are encased in ice. SPID is however de-

signed to measure the free particles in the warm winter mesosphere directly. It is a Faraday type detector which is designed in a way, so that small particles follow the airstream through the probe, allowing particles smaller than 2 nm to enter and not get deflected by the airstream.

SPID was launched successfully for the first time on the G-Chaser student rocket on 13th January 2019 at 09:13 UTC+1 from Andya Norway. The probe was situated in the nosecone of the rocket along with another instrument from Japan. The G-Chaser student rocket was a part of the Grand Challenge Initiative; a collaboration between Colorado Space Grant Consortium, NASA Wallops Flight Facility, Andya Space Center and University of Oslo. This was the only student rocket in the program and contained instruments from seven universities from Norway, USA and Japan.
The main objective of this thesis is to study the possible charging effects by ambient plasma and photoemission on the rocket payload as well as the possible influence of the photoemission current being induced on the grids of SPID. In addition several charging models are reviewed and compared to the measured current and the dependence they have on particle parameters. It is also important to examine the total payload charge and the importance of sunlight shining on the probe. First background information is given on the atmosphere and the mesosphere in particular and an overview of MSPs is given. Then some information is given on the G-Chaser rocket mission and the SPID probe design is introduced. Next the theory behind payload charging and induced photocurrent is given and the different charging models chosen are listed. The next two chapters provide an overview of the collected data both from SPID and the flight data is given. Then the last chapter reviews the estimates from payload charging calculations, possible charge of dust inside the probe and the various considerations needed and then how the actual measurements compare with theory. The last chapter contains the conclusion and discussions.

Chapter 2

Meteoric Smoke Particles

Research on meteoric smoke particles(MSPs) has increased in later years due to interest in their possible existence and the connections to several atmospheric processes. Better atmospheric modelling, numerous sounding rocket experiments dedicated to their detection and development of new methods to detect them have been developed. They are thought to be coagulated or re-condensed material from ablated meteors and other constituents in the atmosphere and reside in several layers, depending on season in the atmosphere. This chapter will cover basic information on the atmosphere, meteoric ablation and most important information on MSPs.

2.1 Earth's Atmosphere

The atmosphere is divided into several different layers according to the temperature variations within them. Since the rocket had an apogee of over 180 km it flew through several of these layers. Figure 2.1 shows the neutral temperature and density for the altitude range of 0 to 180 km of the day of the G-Chaser launch. Also shown in the image is the different layers of the atmosphere, the layers on the left side marked in red have arbitrary boundaries depending on the temperature changing sign at the boundary of each. This arbitrary boundary varies with season and atmospheric conditions. The troposphere is the first layer dominated by decreasing temperature with increasing altitude due to thermal radiation outward from the ground to roughly 12 km altitude at the tropopause, marking the boundary between the troposphere and the stratosphere. In the next atmospheric layer from roughly 12 to 55 km, is the stratosphere, the temperature increases here with altitude due to absorption of solar radiation in the UV range by ozone. The stratopause then marks the boundary between the stratosphere and the mesosphere; where the temperature starts to decrease again, similar to the troposphere.

The upper boundary of the mesosphere is called the mesopause; at roughly 85 km where the thermosphere takes over. Here the temperature increases again due to absorption of molecular oxygen in the EUV range and ionisation of atmospheric constituents (Plane et al., 2015). The right side of figure 2.1 shows the neutral number density along with the start of the ionosphere, at roughly 50 km marked in green. This is also an arbitrary boundary with ionisation of neutral constituents. Marked in dashed blue lines is also the different layers of the ionosphere up to 180 km altitude. The D-region starts at 60 km and extends up to 90 km, marking the beginning of the E-region, ending at altitude of roughly 150 km. With the F-1 region from 150 km and onwards which is the main plasma density region.

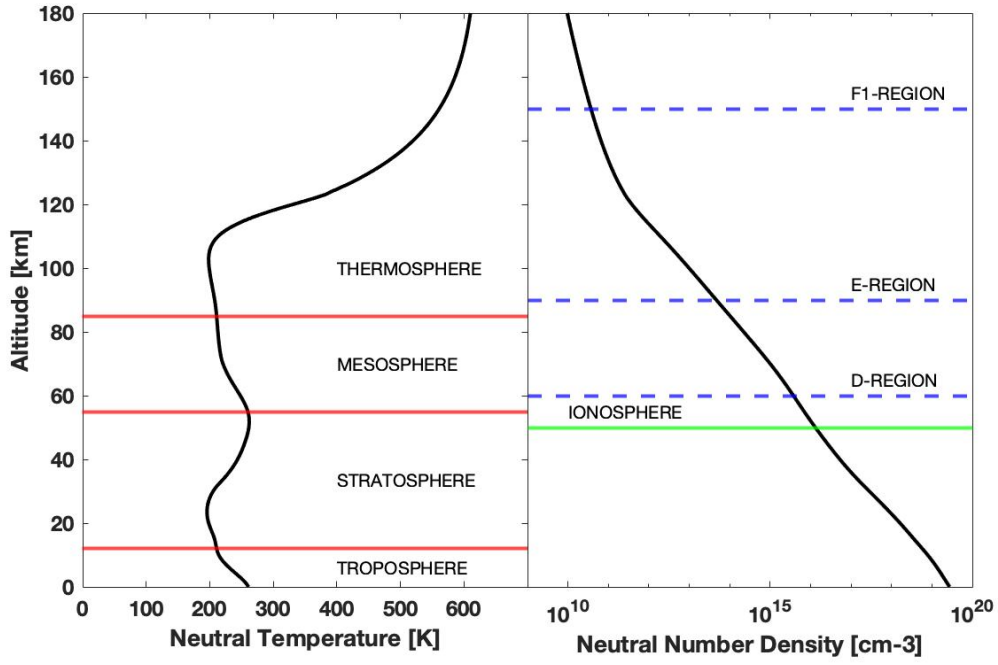

Figure 2.1: Earths different atmospheric layers, atmospheric neutral temperature, neutral number density. Both neutral temperature and neutral density are from the NRLMSISE-00 atmospheric model at time of the G-Chaser launch. Special thanks to Dr. Lutz Rastaetter for providing access to the data (CCMC, Accessed: 2019-05-28)

2.1.1 Mesosphere

The mesosphere is the least studied layer of the atmosphere and it is dominated by large seasonal varaitons. The arbitrary boundaries between the atmospheric layers shift according to their respective temperature variations. Causing the mesopause(its upper boundary) to shift from roughly 70 to 90 km depending on the season(Brekke, 2012). The mesopause is generally regarded as the coldest temperature region in the atmosphere and large seasonal variations as can be seen in figure 2.2. As can be seen from the figure the temperature decreases drastically from the winter season to the summer, possibly reaching temperatures as low as 140 K at 87 km altitude for the north polar region, with a reversed temperature trend for the south polar region (Plane et al., 2015).

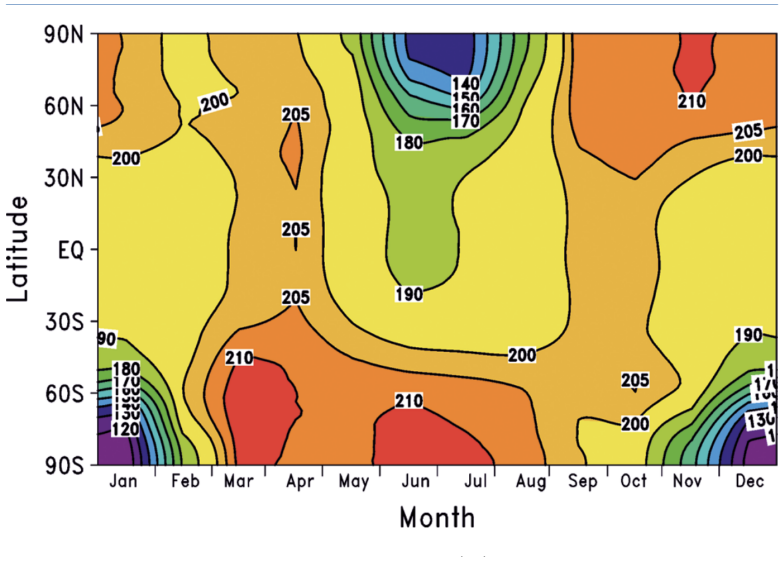

Figure 2.2: Temperature at 87 km altitude for all altitudes and all months of the year. Figure from Plane et al. (2015) - output from WACCM

This large difference in temperature causes the mesospheric region to be quite different from the summer to the winter. And the cold temperature in the summer mesopause causes ice particles to form with sizes of tens of nanometers, most likely with MSPs serving as their condensation nuclei. These particles believed to be a part of the optical phenomenon called Noctilucent Clouds (NLC) and the radar echoes Polar Mesospheric Summer Echoes (PMSE). During the winter the mesosphere is much warmer with no ice particle formation, allowing the MSPs to be detected in-situ by sounding rockets (Antonsen et al., 2017) at altitudes ranging from 50 to 100 km. Due to an effect called polar flux there is a downward flux from equator to the pole causing the altitude distribution of the MSPs to be lower

(Plane et al., 2015). The presence of charged MSPs have been mentioned as a possible connected with Polar Mesospheric Winter Echoes (PMWE), this however remains unknown.

2.1.2 Meteor Ablation

Several tonnes of meteors ablate in the atmosphere every day at altitudes of 70 to 110 km from collisions with the atmospheric constituents with side processes like evaporation and disintegration, depositing meteoric material and metals like Fe, Mg, Si, Na and smaller amounts of Ca and K , materials generally not found in the atmosphere (Plane et al., 2015). This meteoric material then re-condenses in the altitude range 70-120 km to 0.2-2 nm smoke particles(Giono et al., 2018; Antonsen et al., 2017) and as these particles sediment downwards they form possible compounds of oxides, hydroxides and carbonates of nanometer size. The amount of incoming meteoric material is a subject of debate and varies greatly from measurement to measurement, from 3 to 300 tonnes a day, Plane et al. (2015) has reviewed the several methods used and has proposed a more likely 26-44 tonnes per day, however with a 20 tonne uncertainty.
Definitions of the different incoming material by Hunten et al. (1980):

- **meteoroid**: incoming interplanetary particle
- **meteor**: optical and radio phenomena due to a meteoroid interacting with the atmosphere
- **micrometeorite**: a surviving part of a meteoroid that is so small it never reaches melting temperature

Rapp et al. (2012) derived a possible composition and resulting work function of MSPs from several rocket flights. Their measurements detected particle size in the 0.5-3.0 nm size range with generally increasing particle size with decreasing altitude. The work function range they proposed was in the 4-4.6 eV range. Which they concluded indicated Fe and Mg hydroxide-clusters, rather than metal silicates as the major constituents of the smoke particles. With the composition based on the overall input material from meteoroids in combination with atmospheric constituents. From model calculations done by Baumann et al. (2015) based on the original model of Megner et al. (2006) the size and number density distribution of MSPs can be derived for September conditions. The result is shown in figure 2.3 The number density of MSP radius is plotted for negative, neutral and positive particles for similar solar conditions as the G-Chaser launch (with solar elevation 5 °below the horizon - will be discussed in subsequent chapters). This shows a large total neutral number density at altitudes of 80 to 95 km, similar the height

region of the negatively charged particles. The positively charged particles seem to reside at a much lower altitude at about 60 to 80 km but with a much lower concentration. Unfortunately the model is not reliable for altitudes below 60 km and thus is not included in the plot. Comparing these concentrations with figure 2.4 the concentration during the winter (DJF) above 60 °N show a larger total number density of MSPs at lower altitudes compared with summer(JJA) conditions. This might suggest that measuring a higher concentration of MSPs at lower altitudes with larger particle sizes is possible for the launch conditions.

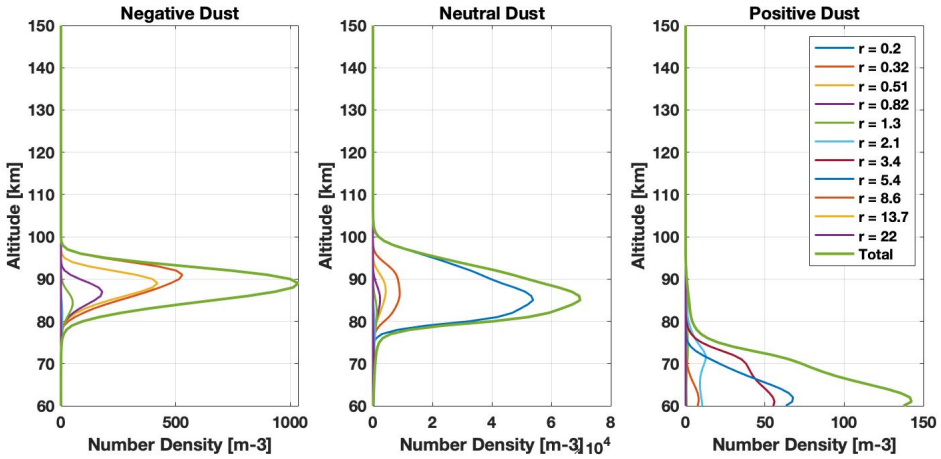

Figure 2.3: Number densities for 11 size bins with radius ranging from 0.2-22 nm, of positive, negative and neutral smoke particles. Plotted from data provided by Baumann et al. (2015), based on a model by Megner et al. (2006).

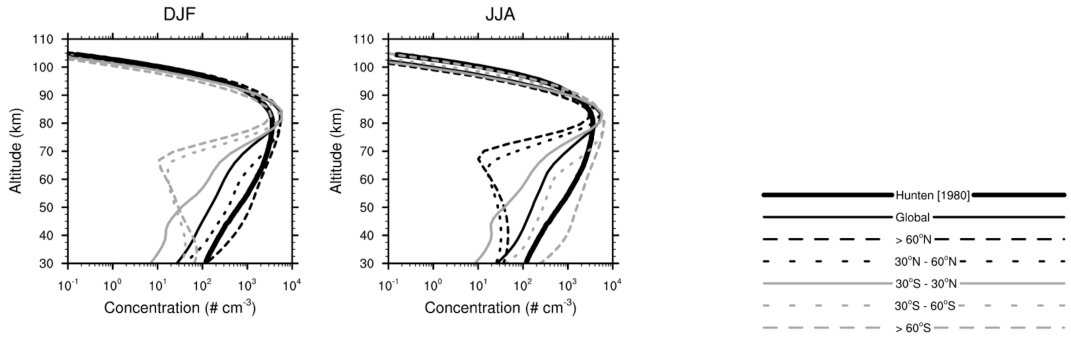

Figure 2.4: Comparison of the concentration of MSPs between winter (DJF) and summer (JJA) with focus on the dashed line representing ¿60°N which should resemble the conditions of the rocket launch at latitude above 69 °N. Figure from Bardeen et al. (2008)(Open Access)

Chapter 3

Background

3.1 G-Chaser

G-Chaser is a student rocket launched as part of the RockSat-XN program and Grand Challenge Initiative in partnership with Wallops Flight Facility and Andya Space Center. It is designed to allow students at a university level to design and launch an experiment. Allowing them to get hands on experience in rocket mission participation, instrument/experiment design, and understanding the challenges scientific return from rocket missions. As part of the process the student teams must participate in several design reviews and deliver certain material on time. With each design review the idea behind the instrument/experiment is further developed and getting more and more closer to the final product. This also ensures that NASA knows what each team is doing and if they are on track. The rocket type used for the G-Chaser launch was a Terrier Improved Malemute, a two stage rocket designed by NASA. Figure 3.1 shows the payload section of the rocket, with the initials of each university marking the placement of their instrument. The top deck is shown on the right with UIT marking the place for the SPID instrument; sharing the nose cone section with the Japanese team instrument PARM. Other universities participating in the rocket launch were the University of Oslo (collaborating with Andya Space Center), University of New Hampshire, Pensilvania State University, University Of Puerto Rico and JAXA and Nagoya University (PARM).

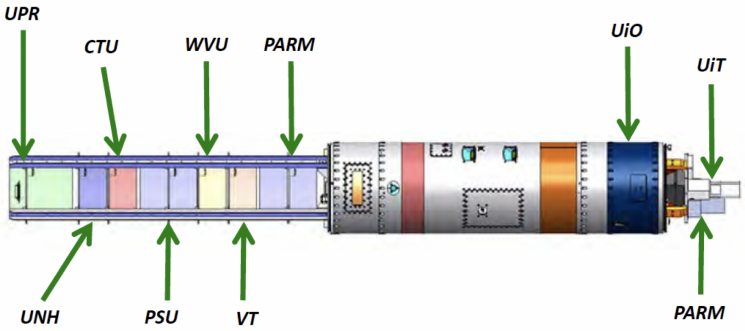

Figure 3.1: Payload section of the rocket. SPID marked with UIT location in the top deck along with PARM the Japanese team. Teams VT and WVU did not end up flying on the rocket. Figure: Chris Koehler, Colorado Space Grant Consortium

3.2 Smoke Particle Impact Detector - SPID

SPID was designed and built by the University of Troms and launched for the first time on the G-Chaser rocket. It is an impact probe and a faraday cup, designed to measure nanometer-sized smoke particles during the winter. The probe was situated in the top deck to be exposed to the airflow and its design is open so as to allow for the smaller particles to get through the shock-front and enter the probe.

3.2.1 SPID heritage: DUSTY and MUDD

SPID is designed with previous impact probes in mind. The University of Troms has previously built and launched the probes DUSTY and MUltiple Dust Detector (MUDD). Both are faraday-cup probes designed to measure ice particles in the cold summer mesosphere. Both probe designs have been launched previously on several rocket missions, DUSTY first and then MUDD as a modified design to the DUSTY design (Havnes et al., 2014; Antonsen et al., 2017). Figure 3.2 shows a schematic of the two probe designs.

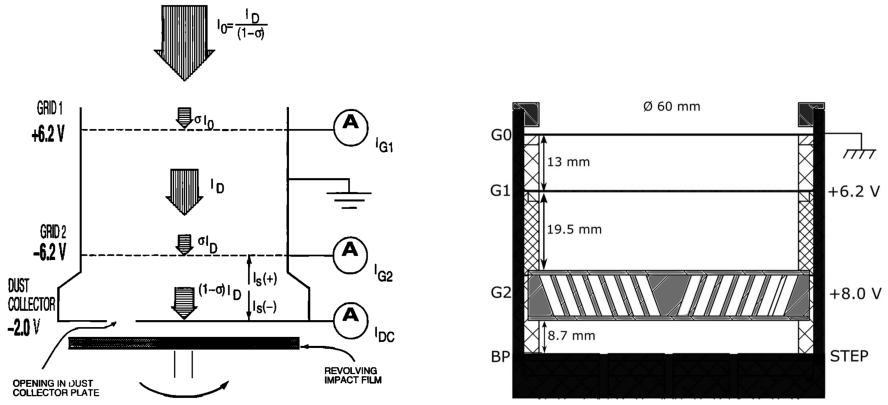

(a) DUSTY (b) MUDD

Figure 3.2: SPID heritage instruments MUDD and DUSTY a) DUSTY probe (Havnes et al., 1996) b) MUDD probe (Antonsen et al., 2017)

Both DUSTY and MUDD have grids at the entrance of the probes with bias potentials to shield out the ambient plasma, DUSTY then has a bottom plate that measures colliding ice particles. The change in the MUDD design was adding the middle plate grid made of inclined concentric rings, so that incoming ice particles will collide with the grid, causing the particles to fragment, releasing the several smoke particles that are thought to be encased within them. These particles are then measured on the bottom plate of MUDD that has a varying potential setting to be able to discern between the particles charge and sizes. The main difference between SPID and the two other designs is that SPID is open to allow for airflow through the probe and is made to measure particles in the warm winter mesosphere when the MSPs are not encased in ice like in the cold summer mesosphere. SPID also has two wire grids to shield out the ambient plasma and a middle plate of concentric rings, but instead of fragmenting ice particles, the middle plate utilizes the triboelectric charging effect when the small smoke particles collide with high speed onto the plate, rubbing of electrons in the process.

3.2.2 SPID Design

SPID is designed to measure very small particles by allowing the airflow in-front of the rocker to enter and flow through it. Figure 3.3 shows a mechanical drawing of the probe, a cylinder with several grids and an opening in the bottom. This opening allows the MSPs to enter the probe and be measured. To measure the particles the probe has an inclined impact grid, the smoke particles collide with the grid and utilizes the triboelectric effect between the particles and the grid to generate a current measured by the probe. The probe also has several wire grids

to shield out the ambient plasma.

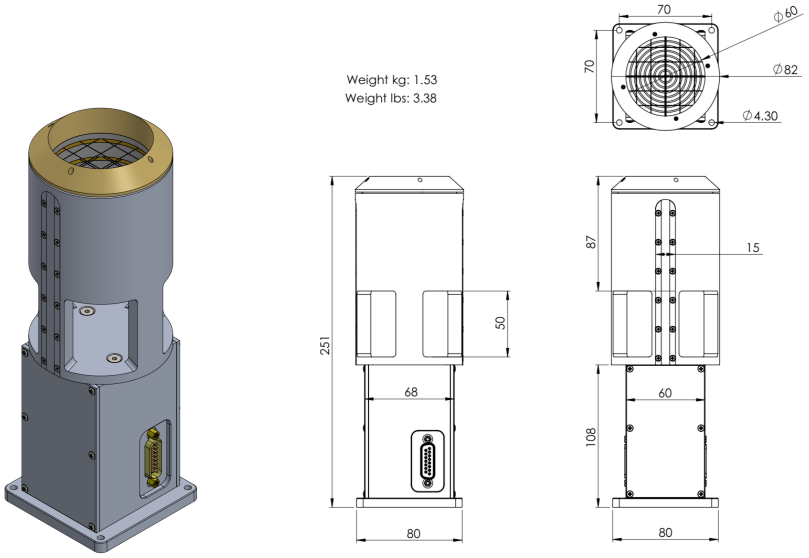

(a) SPID drawing (b) SPID outside dimensions

Figure 3.3: SPID probe 3D drawing and outside dimensions. Drawing from Solidworks by UIT/Sveinung Olsen

A cross-section view of the probe is given in figure 3.4, the placement of the grids and dimensions relative to each other can be seen. A complementary table is given below (table 3.1) where an overview of the different materials used for the probe are given. Also in the table is the potential setting for each grid. The top grid has + 10 V bias potential to shield out the ambient ions, the next grid has a - 10 V, to shield out the ambient electrons. Then comes the middle plate, with a bias potential of -2V and then again there are two thin wire grids of +10 V and -10 V to shield out the ambient plasma from entering from the other side. By shielding out the ambient plasma in theory only the MSPs should enter. The potential setting is the bias potential voltage on each grid relative to the rocket payload ground. This implies that if the rocket becomes charged negatively or positively the ground of the rocket will shift, however the potential of the grids will always stay the same compared to the rocket, no matter how much the paulaod potential might vary.

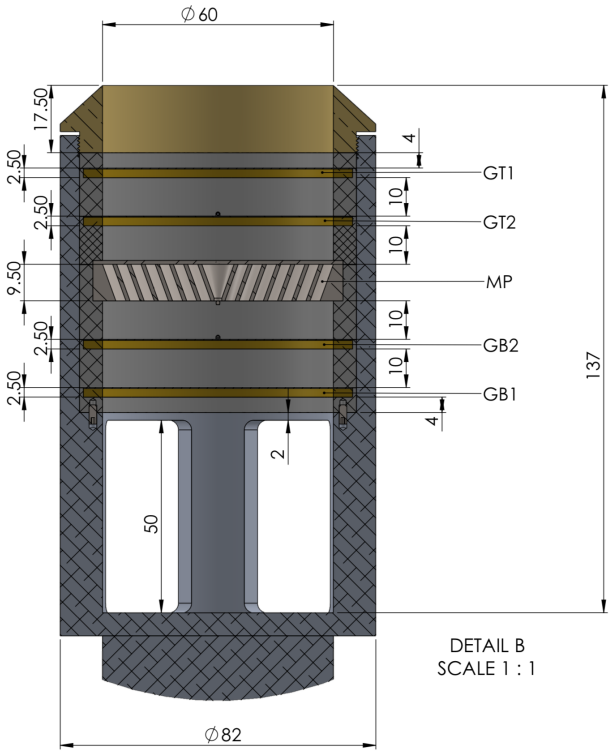

Figure 3.4: Cross section of SPID with dimensions between the grids inside the probe. Drawing in Solidworks by Sveinung Olsen

Table 3.1: SPID probe material and potential setting for the probe grids. Based on information from solidwork drawings by UIT

Part	**Material**	**Potential Setting**
Grid Top 1	Brass coated with silver	$+10V$
Grid Top 2	Brass coated with silver	$-10V$
Middle Plate	AISI Type 316L Stainless Steel	$-2V$
Grid Bottom 1	Brass coated with silver	$+10V$
Grid Bottom 2	Brass coated with silver	$-10V$
SPID Grid holder	Aluminium 6082-T6	NONE
Locking Ring	A4 Stainless Steel	NONE
Part	**Dimensions**	**Potential Setting**

The middle plate is made up of stainless steel, with a large ring and seven other concentric rings, fixed together by stainless steel pins on top of the grid as well as on the bottom. The rings are carved from one solid steel pice with a circular motion, moving over the steel several times to smooth it as much as possible. The smaller grids are made with brass wires coated with silver. All the four silver grids are made in the same manner and are inserted into the probe so that they overlap each other very well. Figure 3.5 shows the middle plate grid as well as one of the silver grids prior to assembly with the rest of SPID.

(a) Middle Plate - Stainless Steel

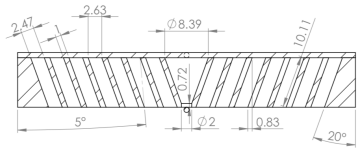

(b) Example of top and bottom silver grids

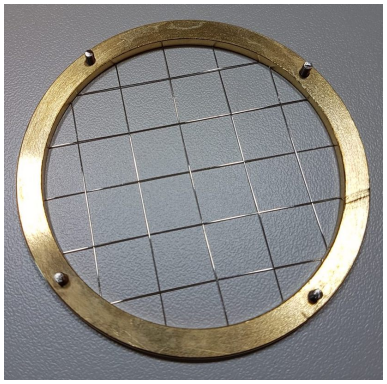

(c) Middle Plate - Stainless Steel

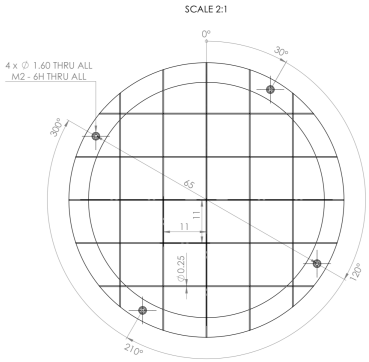

(d) Example of top and bottom silver grids

Figure 3.5: Middle plate and silver coated brass grids prior to assembly. Figure: Sveinung Olsen

Figure 3.6 shows the top deck/nose cone section after final integration at Andya in January of 2019 with SPID and the JAXA/PARM instrument; a field of view camera designed to measure high energetic electrons connected to pulsating auroral event.

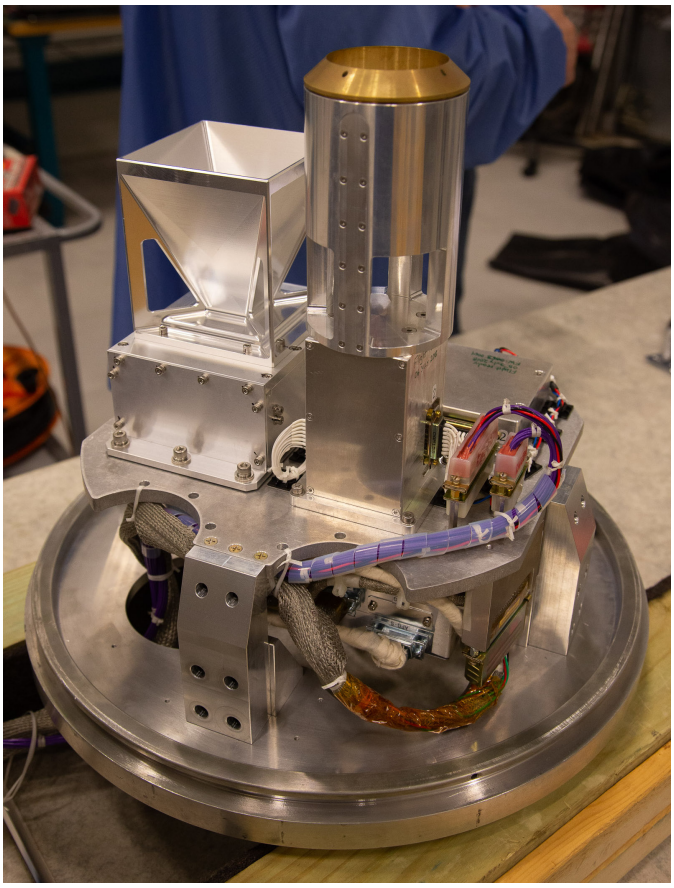

Figure 3.6: Image of SPID and PARM on the top deck, at Andoya Space Center for final integration and testing prior to launch- Figure: NASA/Wallops Flight Facility

Chapter 4

Payload Charging

As the rocket flies through the different layers of the atmosphere it and the payload will become charged. This charging is due to the ambient electrons and ions, photo-emitted electrons due to photons from the solar flux, secondary electron emission and backscattered electrons. All of these factors charge the rocket either positively or negatively, which will alter the rocket potential. The total charge contribution I_T to the surface of the rocket is then the sum of all the charging factors, given by the following equation (called current balance equation): (Darian et al., 2017).

$$I_T(\Phi_s) = I_e(\Phi_s) - I_i(\Phi_s) - I_{ph}(\Phi_{se}) - I_{bse}(\Phi_s) \tag{4.1}$$

Where $I_e$and I_i is the contribution from the ambient plasma electrons and ions. I_{ph} is the resulting electron photocurrent from UV photons incident on the rocket and I_{bse} is both the secondary electron emission and backscattered electrons. The contribution form the I_{bse} will be considered negligible due the larger relative size of the other currents. The resulting current to the rocket will predominantly be negative, especially for altitudes above 70 km since the contribution from fast electrons will dominate (Darian et al., 2017). The current from the ions as well as the photocurrent will charge the payload positively but to a lesser extent. In the rest of the chapter the currents from the ambient plasma as well as the photocurrent will be examined in detail.

4.1 Charging due to Ambient Plasma

As long a the rocket radius is larger than the Debye length the incident ion current to the rocket surface can be calculated with the following equation: (Darian et al., 2017)

$$I_i \approx \alpha n_i e v_B A \tag{4.2}$$

Where α is dependent of the temperature ratio of the electrons and ions T_e/T_i, n_i is the ion number density, e is the elementary charge, A is the surface area of the rocket v_B is the Bohm velocity, and is given by:

$$v_B = \sqrt{\frac{k_B T_e}{m_i}} \tag{4.3}$$

Where k_B is the Boltzmann constant, T_e is the electron temperature and m_i is the mass of the ions.
The current due to the electrons is given by: (Darian et al., 2017)

$$I_e \approx -\frac{1}{4} n_e e \ \overline{v_e} A \ exp\Big(- \frac{e|\Phi - \Phi_{pl}|}{k_B T_e} \Big) \tag{4.4}$$

Where n_e is the electron number density, Φ is the electric potential in the sheath region, and Φ_{pl} is the potential of the undisturbed plasma far away. (can arbitrarily set to zero).
$\overline{v_e}$ is the mean electron velocity given by:

$$\overline{v_e} = \sqrt{\frac{8 k_B T_e}{\pi m_e}} \tag{4.5}$$

4.2 Photoemission/Photocurrent

When an object is exposed to the solar flux without the protection of the atmosphere, some parts of the solar spectrum will influence the material by way of photons interacting with the material and ejecting electrons. This will cause the payload to gain a positive charge; and this is the case for space crafts in orbit around earth. When in direct sunlight they will usually charge up to a positive potential. Sounding rockets are also affected by the photocurrent generated but to a lesser extent, this is due to the absorption of large parts of the solar spectrum by the atmosphere. Sounding rockets will also become negatively charged due to the ambient electrons, with the photocurrent and ambient ions deceasing the total negative charge by a small fraction. This section will go over the main factors in estimating the photocurrent, the source of the incident photons; the solar spectrum, the amount of direct sunlight in the atmosphere, the absorption of the sunlight by main constituents in the atmosphere and how the photons interact with different materials, with focus on the materials used for the G-Chaser rocket.

4.2.1 The Solar Spectrum

The sun is essentially a black body and the solar spectrum can be estimated as a black body spectrum with surface temperature of around 6000 K. As can be seen

from figure 4.1 the solar irradiance varies with the incident photon wavelength. The marked portion of the spectrum is the UV range of the irradiance, this part of the spectrum is the most varied, and is very dependent on the conditions of the sun. Meaning there is large variation in the spectrum reaching the top of the atmosphere for high or low solar activity. This is also illustrated in figure 4.2, which shows the ratio of the solar spectrum measured in February 1979(high activity/normal) to the spectrum measured in July 1976(low activity), showing the largest variation in the UV range/part of the spectrum compared to the rest of the spectrum continuum. This is due to the flux from the sun in the UV wavelength range is from the hottest regions of the atmosphere of the sun with solar flares causing an even larger variation(Rees, 1989; Lean, 1997). As the spectrum from the sun enters the atmosphere some parts of it get absorbed by different constituents. Several satellites that reside outside Earths atmosphere measure the solar radiation, this can be used to measure the total absorption in the different wavelength regimes of the spectrum. The UV range of the spectrum gets largely absorbed above 80 km with variations within the spectrum and thus influences several processes in the atmosphere(Rees, 1989).

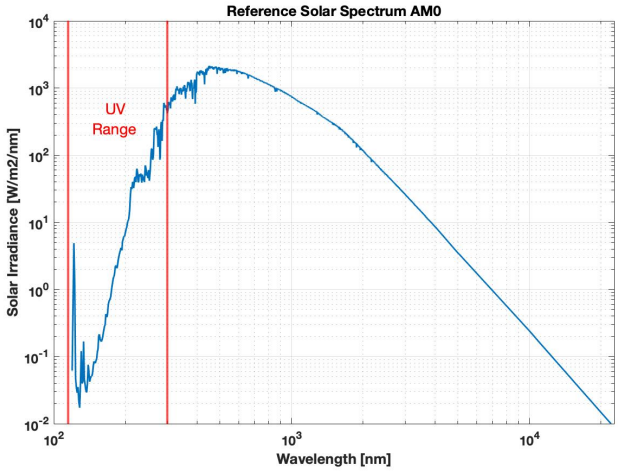

Figure 4.1: Reference solar irradiance spectrum per wavelength in nanometers above earths atmosphere (often called AM0). Marked in red is the UV portion fo the solar spectrum. Plotted with data from (NREL, Accessed: 2019-05-22)

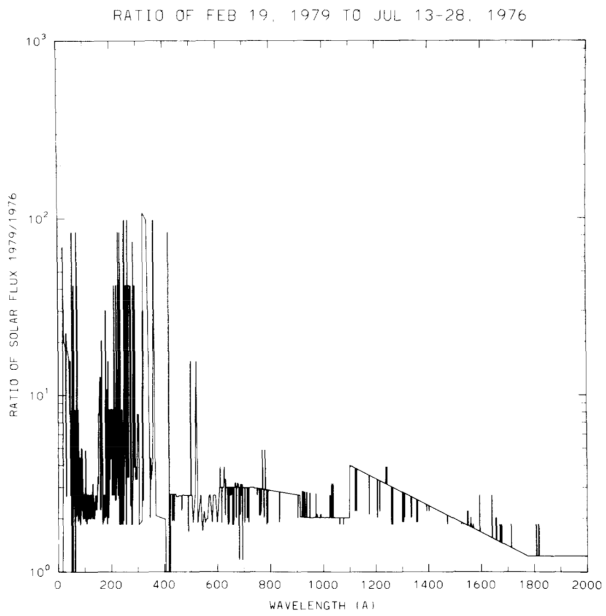

Figure 4.2: Ratio of solar spectrum measured on 19 of February 1979 to 10 of July 1976, the latter observation was at a very low solar activity with almost no sunspots visible on the suns surface. Reprinted from Planetary and Space Science,Vol 31/Issue 6, R.G Roble and B.A Emery, On the global mean temperature of the thermosphere, Pages 597-614., Copyright (1983), with permission from Elsevier.(Hinteregger, 1981; Roble and Emery, 1983)

4.2.2 Atmospheric Absorption and Optical Depth

As the irradiance from the sun enters the atmosphere, parts of it gets absorbed by different atmospheric constituents at different wavelengths of the incident solar flux. How the radiation is transported throughout the atmosphere can be described by the Lamber-Beer law which is given by the following equation: (Rees, 1989)

$$I(\lambda) = I_{\infty}(\lambda)e^{-\tau(\lambda)} \tag{4.6}$$

Where $\tau(\lambda)$ is the optical depth. and $I_{inf}(\lambda)$ is the solar irradiance at the top of the atmosphere for each wavelength λ which can be obtained from satellite measurements. The main area we are interest in is the UV spectrum from 115 - 300 nm since the photocurrent from other regions of the solar flux on most materials can be considered negligible (Giono et al., 2018). Noteworthy parts of this wavelength region is the Lyman-alpha line at 121.56 nm, with in general a much higher irradiance spectrum than the surrounding continuum. The optical depth $\tau(\lambda)$ specifies how much the atmosphere reduces the magnitude of the solar irradiance for a specific earth and sun geometry and atmospheric conditions and

constituents. The basic equation of optical depth for an overhead sun (solar zenith angle is zero) is given by (Rees, 1989):

$$\tau^{v}_{z_0}(\lambda) = \sum \sigma^{a}_{j}(\lambda) \int_{z_0}^{\infty} n_j(z) dz \tag{4.7}$$

Where $\sigma^{a}_{j}(\lambda)$ is the absorption cross section of species j for each wavelength λ, $n_j(z)$ is the number density of each atmospheric constituent being considered and z_0 is the altitude being considered at each integration value. Figure 4.3 the geometry for a solar zenith angle, χ_0, larger than 90 °is shown. This geometry results in the following equation for the optical depth: (Rees, 1989)

$$\tau(\lambda, z_0, \chi_0) = \sum_j \sigma^{a}_{j}(\lambda) \Bigg\{ 2 \int_{z_a}^{\infty} n_j(z) \left[1 - \left(\frac{R + z_s}{R + z} \right)^2 \right]^{-1/2} dz \tag{4.8}$$

$$- \int_{z_0}^{\infty} n_j(z) \left[1 - \left(\frac{R + z_0}{R + z} \right)^2 sin^2(\chi_0) \right] dz \Bigg\} \tag{4.9}$$

With R being the radius of the Earth and z_s is a screening height with the atmosphere being opaque below it (Rees, 1989). So in order to calculate the optical depth in the atmosphere at the time of the launch the solar zenith angle must be known, the atmospheric constituents dominating the absorption and their respective number density and absorption cross sections. This can be obtained from atmospheric models like NRLMSISE-00 (CCMC, Accessed: 2019-05-28) that can provide neutral number density and neutral temperature profiles for desired altitudes. The absorption cross sections can be obtained from numerous literature, this is however a challenge since not all the measurement agree and many experiments do not measure in the entire wavelength region that is interesting, here the 115-300 nm range.

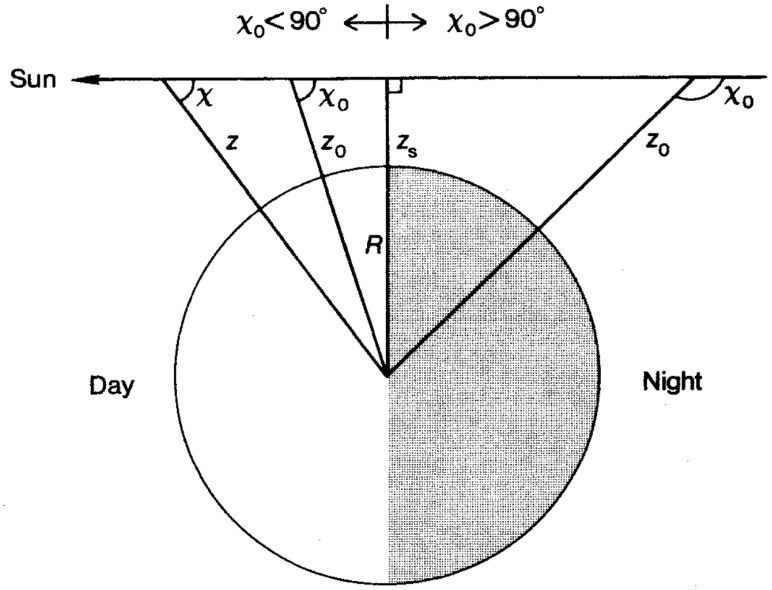

Figure 4.3: Geometry for calculating the optical depth,χ_0, at the location of the rocket launch. Not to scale. We are Interested in when the solar zenith angle is $\chi_0 > 90$. Reprinted from Physics and Chemistry of the Upper Atmosphere, M. H. Rees, Copyright (1989), with permission of Cambridge University Press through PLSclear.

Other properties that need to considered in calculating the photocurrent induced in a material is the photoelectric yield and its total reflectance or absorption for different wavelengths. The photoelectric yield is the probability of ejecting electron by the incident photon on the material, and if the photon has enough energy to do so, this factor also depends on the condition of the surface and its structure and composition. The reflectance depend on the reflection properties of a material(Giono et al., 2018). It is also important to consider the angle of which the sun falls on the material with the electron generation being highest at 0 ° incidence and goes down as a function of cosine of the incident angle. However for the purpose of calculating an estimated photocurrent it can be assumed to be incident at a 0 ° angle. The method to calculate the resulting photocurrent is given by Giono et al. (2018). The absorption of a material can be calculated from its total reflectance from the relationGiono et al. (2018):

$$R_A = 1 - R_T(\lambda, \theta_i) \tag{4.10}$$

Where θ_i is the incident angle of illumination and λ the incident wavelength. To

calculate the total reflection the Fresnel equations can be used find for s and p polarisations s and p polarised reflectance coming from one medium with reflection index n_1 incident on another medium with refractive index n_2 and are given by the following equations for s and p polarisation:

$$R_s = \left| \frac{n_1 cos\theta_i - n_2\sqrt{1 - (\frac{n_1}{n_2} sin\theta_i)^2}}{n_1 cos\theta_i + n_2\sqrt{1 - (\frac{n_1}{n_2} sin\theta_i)^2}} \right|^2 \tag{4.11}$$

$$R_p = \left| \frac{\sqrt{1 - (\frac{n_1}{n_2} sin\theta_i)^2} - n_2 cos\theta_i}{\sqrt{1 - (\frac{n_1}{n_2} sin\theta_i)^2} + n_2 cos\theta_i} \right|^2 \tag{4.12}$$

And since we are interested in reflection of sunlight from air we can set its refractive index as $n_1 = 1$ and the resulting equations becomes Giono et al. (2018):

$$R_s(\lambda, \theta_i) = \left| \frac{cos\theta_i - n(\lambda)\sqrt{1 - n(\lambda)^{-2} sin^2\theta_i}}{cos\theta_i + n(\lambda)\sqrt{1 - n(\lambda)^{-2} sin^2\theta_i}} \right|^2 \tag{4.13}$$

$$R_p(\lambda, \theta_i) = \left| \frac{\sqrt{1 - n(\lambda)^{-2} sin^2\theta_i} - n(\lambda) cos\theta_i}{\sqrt{1 - n(\lambda)^{-2} sin^2\theta_i} + n(\lambda) cos\theta_i} \right|^2 \tag{4.14}$$

Here the equations are given as a function of the wavelength of the incident wave as well as the incidence angle and $n(\lambda)$ is the refractive index of the material the sunlight is incident on. The total reflectance is then given by the average of the two polarisations and then the absorption of a chosen material can be calculated if its refractive index is known for the specific wavelength range:

$$R_T(\lambda, \theta_i) = \frac{R_p(\lambda, \theta_i) + R_s(\lambda, \theta_i)}{2} \tag{4.15}$$

4.2.3 Solar Zenith Angle

In order to accurately calculate the amount of photocurrent produced by the sun on the rocket payload the solar zenith angle must be calculated. The solar zenith angle is the angle the sun makes with the surface normal. This means that an overhead sun will have a solar zenith angle of 0 degrees and a setting sun will have a solar zenith angle of 90 degrees. Since the rocket is launched in January at Andya, the sun will never rise above the horizon and the solar zenith angle will be larger than 90 degrees. The altitude of direct light can then also be calculated. This section is about how to calculate the solar zenith angle for the time of the rocket launch for a given latitude and longitude and time of day. As well as the

minimum altitude of direct sunlight. The solar zenith angle θ_Z can be calculated with the following equation:

$$cos(\theta_Z) = sin(\delta)sin(\phi) + cos(\delta)cos(\phi)cos(\omega_H); \tag{4.16}$$

Where ϕ is the local latitude, ω_H is the hour angle and δ is the declination angle. Which is the angle between the earth and sun plane compared to earths equator (Solanki, 2015) and is given by:

$$\delta = 23.45 * sin\Big(\frac{360}{365}(284 + n)\Big) \tag{4.17}$$

Where n is the day of year (DOY)($n = 13$ for january 13).
The hour angle is a measure of when during the day the sun will rise and set compared to noon time and is calculated in the following way:

$$\omega_H = 15(LST - 12) \tag{4.18}$$

Here the 15 stands for degrees per hour, since earth rotates 360 ° roughly every 24 hours, then 1 hour equals 15 degrees (Solanki, 2015). LST is the Local Solar Time and is given by:

$$LST = LT + \frac{TC}{60} \tag{4.19}$$

Where LT is the local time(in hours and fraction of an hour) and TC is the Time Correction Factor and is given by:

$$TC = 4 * (Longitude - LSMT) + EoT \tag{4.20}$$

The factor of 4 stands for minutes (earth rotates 1° every 4 minutes), EoT is the Equation of Time and LSMT is the Local Standard Time Meridian and is given by

$$LSMT = 15 * \Delta T_{GMT} \tag{4.21}$$

With ΔT_{GMT} being the the difference of the Local Time (LT) from Greenwich Mean Time (GMT) in hours. The equation of time EoT is due to fluctuations in earths rotational speed causing the calculated solar time to vary slightly compared to the local time (Solanki, 2015) and can be calculated with the following equation:

$$EoT = 9.87 * sin(2B) - 7.53cos(B) - 1.5sin(B) \tag{4.22}$$

With B being a constant given by:

$$B = \frac{360}{365}(n - 81) \tag{4.23}$$

The elevation angle α can now be calculated with the following equation:

$$\alpha = 90 - \theta_Z \tag{4.24}$$

And the minimum altitude of direct sun can now be calculated using cosine relations:

$$h_{sun} = R_E\Big(\frac{1}{cos(\theta_Z) - 1}\Big) \tag{4.25}$$

Where R_E is the radius of the earth and θ_Z is the solar zenith angle from above.

Chapter 5

Collisional Dust Charging

The current measured on the grids depends then on the probability of the particles to collide with the middle plate, their composition and initial charge. By comparing the measured signal with the signal predicted by theory for different compositions we might be able to deduce relevant information about the particles such as size, charge and possible composition. Charging of the particles in the probe depend on the original charge when the particles enter the probe as well as their size. The larger the particles the more charge they can gain by triboelectric charging. This however has some limitations, the particles cannot gain infinite amount of charge and their size limits this amount. This chapter will go over the process of triboelectric charging and the different charging models available to define a small particle collisions with a surface.

5.1 Triboelectric Charging

The theory of triboelectric charge transfer was first discussed/theorised in 1779 by Volta, this theory was furthered by Helmholz in 1879 and the Volta-Helmholz hypothesis was formed. This hypothesis stated that materials when in contact could cause electric charge to flow between the bodies due to friction and a double layer that forms when they are brought into contact (Harper, 1951). The Volta-Helholz hypothesis ordered materials in series, and states that the charge transfer between two materials in that series is dictated by their respective order, and that the contact potential established between the two materials was connected to this double layer and the possible energy levels of the materials. Harper (1951) suggested that the energy levels would determine if the material would become positive or negatively charged as a result of the contact and called this phenomenon separation charging. This separation charge is now determined by the work function of a material; which is a measured quantity for each material and is often measured

with photoemission. So in order for a photon to eject an electron from a material it needs to overcome the threshold energy which is the work function (Matsusaka et al., 2010). So when two materials with different work functions are brought into contact their fermi levels are different as can be seen in figure 5.1, electrons will start to flow between the two materials (by way of tunnelling), they will flow from the material with a higher work function to the material with a lower work function until the fermi levels are equal. The amount of energy that flows between then is given with the formula(Harper, 1951; Matsusaka et al., 2010).:

$$V_c = (V_{1/2}) = -\frac{\phi_1 - \phi_2}{e} \tag{5.1}$$

Where V_c is the contact potential difference of metal 1 against metal 2, ϕ_1 is the work function of metal 1 and ϕ_2 is the work function of metal 2, e is the elementary charge.

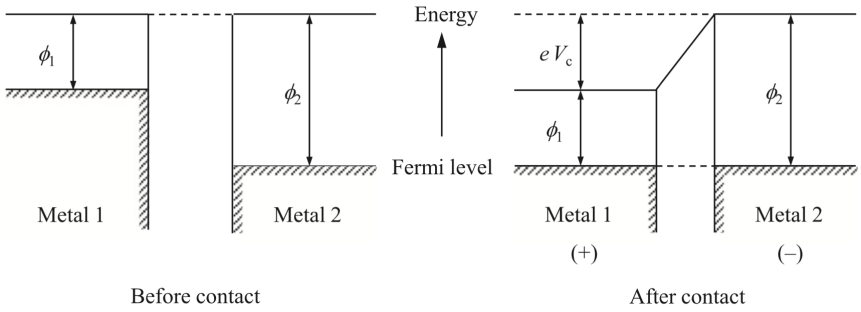

Figure 5.1: Showing the main mechanisms behind metal to metal contact for metals with different work functions. (Matsusaka et al., 2002, 2010) Reprinted from Chemical Engineering Science,Vol 65/Issue 22, S.Matsusakaa, H.Maruyamaa, T.Matsuyama and M.Ghadiric, Triboelectric charging of powders: A review, Pages 5781-5807, Copyright (2010), with permission from Elsevier.

The total charge Q_c that is transferred in the collision is given by the following relation (Matsusaka et al., 2010):

$$Q_c = C_0 V_c \tag{5.2}$$

Where C_0 is the capacitance between the metals at a certain critical separation distance, which is the distance between them at the moment the charge transfer stops. This capacitance between the metals is the one that varies between different charging models, two metals can be considered as two parallel plate capacitors to calculate the capacitance, however since in the case of small dust particle colliding with a large surface the capacitance needs to be adjusted accordingly. Experiments

have shown that several factors can influence this that need to be considered, especially due to high theoretical values compared to experiments, these factors can include condition of the surface, oxidation layer and impurities among others (Harper, 1951; John, 1995; Matsusaka et al., 2010). The charge transferred in the contact is also dependent on other factors, like if the particle is charged prior to collision. The total charge Q_T transferred is given by: (John, 1995)

$$Q_T = Q_c + Q_t = Q_c + Q_0 \tag{5.3}$$

Where Q_t is the pre-charge pf the particle transferred to the surface at the moment of contact between the particle and the surface.

5.2 Charging Models

Several different charging models exist for small particles, most of these never consider particles below the micro meter range and many struggle to experimentally correlate their theories. This section will give a brief overview of the charging models considered for the charging of small dust particles in SPID.

5.2.1 Adams & Smith - 1970

The paper by Adams and Smith (1971) gave a simple model based on ratios between particle mass and velocity and the resulting generated charge. This charging model is chosen since it does not include the work function of the particles, any particle properties other than radius and density and can be compared to the other charging models that do. This was done since there are so large uncertainties considering composition and size of MSPs, which generated a large uncertainty in subsequent models and it serves a s a comparative model to charge generation. The main downside of this model is that it was developed and experimentally tested for micrometers sized particles and not nanometer sized. The following relation ship between the resulting charge q of the impact and the velocity v and mass m of the particles considered is given by:

$$Q_c = Km^{\alpha}v^{\beta} \tag{5.4}$$

Experimental result using iron particles showed values of roughly $\alpha = 1$, $\beta = 3.2$ and $K = 0.88$ and since iron is a possible composition of MSPs this should be considered. The mass can be calculated from the density ρ and the particle radius :

$$m = \frac{4\pi}{3}\rho r^3 \tag{5.5}$$

5.2.2 Walter John - 1995

John (1995) has developed a more detailed charging model for the generated impact charge. This model accounts for the potential difference between the particles and the surface, the separation distance between them, mechanical properties of both particle and surface. The equation is off the form given in equation 5.2 with a complex expression for the capacitance between them. He gives a general form for contact charge as:

$$Q_c = \frac{\pi\epsilon_0 V_c}{Z}\left[\frac{5}{4}\pi^2\rho v^2(k_p + k_s)\right]^{2/5} \times a^2(1 - e^{-\Delta t/\tau}) \tag{5.6}$$

Where ϵ_0 is the permittivity i free space, V_c si the contact potential, Z is the separation between the particles and the surface, ρ is the particle density, v is the impact velocity, r is the particle radius, Δt is the duration of the contact, τ is the charge relaxation time of the particle. The mechanical constants k_p for the particle and k_s for the surface are defined in the following way:

$$k = \frac{1 - \upsilon^2}{\pi E} \tag{5.7}$$

Where υ is the Poisson's ratio and E is the young's modulus for a chosen material. Equation 5.6 can be further defined for a metal to metal contact, by assuming that both the surface and particles are metallic conductors:

$$Q_c = \frac{\pi\epsilon_0 V_c}{Z}\left[\frac{5}{4}\pi^2\rho(k_p + k_s)\right]^{2/5} v^{4/5} r^2 \tag{5.8}$$

5.2.3 Matsusaka et al. - 2010

Matsusaka et al. (2010) has developed two charging models in their paper, the Condenser model and the Charge relaxation model. The Condenser model shows more promise for metal to metal contact where as the Charge relaxation model more for insulator to metal contact. The condenser model represents the impact charge as:

$$Q_c = k_c C V_t \tag{5.9}$$

Where k_c is the charging efficiency in the process, and C and V_t are the capacitance and the total potential difference. They propose the following relation for the capacitance C:

$$C = \frac{\epsilon_0 S}{Z} \tag{5.10}$$

Where ϵ_0 is the permittivity of free space, S is the contact area of the particle and the surface as the particle becomes compressed in the collision. The total potential difference here is both dependent on the potential difference V_c due to the difference in work function fo the materials as given in equation 5.1 as well as other added terms given as:

$$V_t = V_c - V_e - V_b + V_{ex} \tag{5.11}$$

Where V_{ex} is a potential due to external electric fields(like the bias potential on the middle plate), V_ba space charge caused by surrounding charged particles. And $V_e$is the potential due to image charge and is given by

$$V_e = k_e q \tag{5.12}$$

Where q is the charge on the particle prior to impact and k_e is given by:

$$k_e = \frac{2Z}{\pi\epsilon_0 D_p^2} \tag{5.13}$$

Where D_p is the particle diameter. Now the impact charge can be written as:

$$Q_c = k_c \frac{\epsilon_0 S}{Z}(V_c - \frac{2Zq}{\pi\epsilon_0 D_p^2} + V_{ex}) \tag{5.14}$$

5.2.4 Wang & John - 1988

Wang and John (1988) give charging models for both elastic and plastic impact. The elastic impact equation they propose is similar to John (1995) with some modifications and thus will not be discussed here. For plastic impacts the charge generated is given by:

$$Q_p = \frac{\pi r \alpha_m \epsilon_0 \psi}{Z} \tag{5.15}$$

Where α_m is the maximum value of deformation that occurs at the moment the of impact and is given by:

$$\alpha_m = 0.5 b_2 + \sqrt{b_1^2 + b_2^2} \tag{5.16}$$

b_2 and b_2 are constants and are given by

$$b_1 = \frac{8\pi^2 r^2 P_y^2}{27 {C_k}^2} \tag{5.17}$$

$$b_2 = V_1 \sqrt{\frac{m}{P_y \pi r}} \tag{5.18}$$

Where P_y is the yield pressure for the particles, denoting the pressure the material can handle before plastic deformation occurs, r is the particle radius, m is the mass of the particles and C_k is a constant (not to be confused with the capacitance) and is given by

$$C_k = \frac{4\sqrt{r}}{3\pi(k_p + k_s)} \tag{5.19}$$

V_1 is the particle velocity at impact and can be set equal to the yield velocity V_y given by:

$$V_y = V_i \left[1 - \frac{1\pi^8 P_y^5 (k_s + k_p)^4}{40 V_i^2 \rho_p} \right]^{1/2} \tag{5.20}$$

5.3 Charge Limit

To estimate the charge limit on a on a nanometer sized particle there are two things that need to be considered. The electron field emission limit and the electrostatic disruption limit. Electron field emission occurs when the particle has reached the amount of charge before it starts to emit electrons away. Condition for electron field emission not to occur is: (Mann et al., 2014)

$$Z > -(1 + 0.7 r_{nm}^2) \tag{5.21}$$

Where r_{nm} is the size of the particles given in nm and Z is the charge state. The amount of charge a particle can hold before being ripped apart by large field forces inside it due to the charge on the surface is given by the electrostatic disruption limit Mann et al. (2014),:

$$|Z_{max}| = 7 \times \gamma^{1/2} r_{nm}^2 \tag{5.22}$$

Where γ depends on the material properties of the particles. Where $S_{max} = \gamma \times 10^9 N\ m^{-2}$ represents the extreme bonds of different particle properties. With γ varying from $1e^{-4}$ to 1. And as mentioned by Mann et al. (2014), the maximum limit is reached for fluffy comet material, composed of ice and dirt at $\gamma = 1e^{-4}$ while the limit is met for hard bulk solids and tektites with $\gamma = 1$. Tektites are volcanic material that is melted/evaporated with large heat and then re-condensed. Now this is a similar process as for MSPS, and even though we do not know the composition of MSPs we can assume they are more like the tektites than the

cometary material. This results in a much higher possible charge on the particles than for a lower γ value.

Chapter 6

Flight and Measurement Data

During the rocket flight the SPID instrument collected data from all of the four silver grids as well as the middle plate, this provided five streams of current for the entire flight. Which lasted about 600 seconds total. Including the data from the instrument the attitude section of the payload section, provided by NASA, collected altitude information, measurements from magnetometers, GPS position, power to each instrument section and the velocity and acceleration of the rocket. This chapter will give an introduction of all the measured data with focus on interesting aspects of the rocket flight that can be seen in the data. The flight data included the altitude of the rocket, the latitude and longitude position during the rocket flight, the x, y, z and total velocity vectors and acceleration vectors, along with the total power to the instrument section that SPID was located on. figure 6.1 shows the result of the altitude and position of the rocket. With an apogee of around 184 km during the 600 seconds of flight, from the altitude plot we can see the launch at 0 seconds, and the second stage burn starting at 20 seconds. This data is provided by NASA so the actual information has most likely been smoothed and simplified.

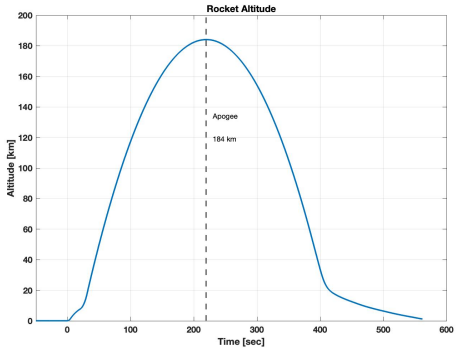

(a) Altitude of the Rocket

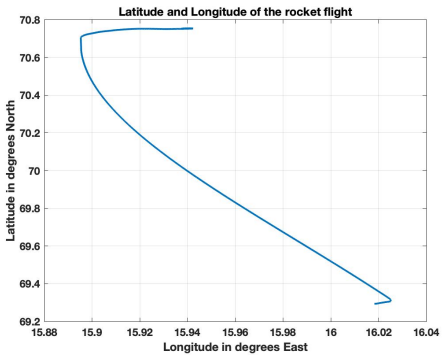

(b) Latitude and Longitude of the Rocket flight

Figure 6.1: On the left is shown the altitude of the rocket with time of flight for the rocket, showing in dashed lines the maximum altitude, with apogee of around 184 km.On the right is the latitude and longitude of the rocket from the GPS measurements from the telemetry measurement section of the rocket, with the launch point being the lowest point of the graph at 69 degrees north and 16 degrees east. The data used to plot the figure is provided by NASA Wallops Flight Facility

Comparison of the altitude and the velocity of the rocket is shown in figure 6.2, where figure 6.2 a) shows the total velocity with the altitude, this is a good comparison to get an idea of some important events during the flight. since the rocket has two stages this can be clearly seen in the total velocity, with the small dot-dashed lines on the left side marking the end of the first and seconds burnout. with the second line showing correlation with the altitude plot. On the right side on part a) we can clearly see the decrease in velocity as the rocket gets slowed down by the increasing amount of atmosphere, stopping the increasing speed being gained by the rocket after apogee. This is around 60 km altitude on the way down.

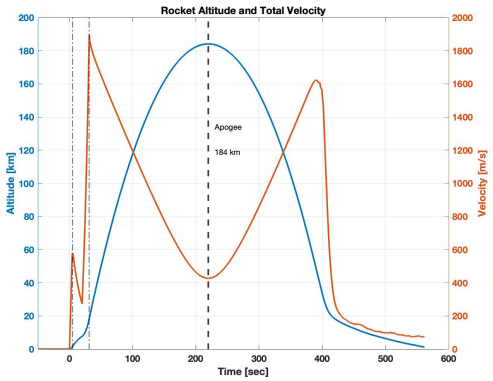

(a) Altitude and total Velocity of the Rocket

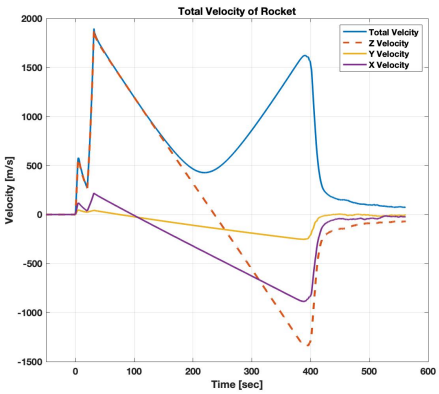

(b) Total velocity plotted with z, x and y velocity vectors.

Figure 6.2: Figure part a) shows the altitude of the rocket plotted with the total velocity with the dashed line marking the apogee as before. The small dot-dashed lines on the left indicate the end for the first and second stage burnouts. of the rocket. Figure part b) shows the total velocity vector compared to the velocity vectors in x, z, and y direction. The data used to plot the figures is provided by NASA Wallops Flight Facility

Figure 6.3 shows the acceleration vectors of the rocket during flight in x, y and z direction of the rocket. Note however that the plots given mark the top direction as the Z direction and the others as x and y. From the graph we can clearly see that the z vector fo the rocket was pointing along the rocket while the two x and y vectors were pointing along the rocket normal. In the plots there are marked the end of first burnout, start and end of the second, the apogee of the rocket and the time wen the rocket first meets the atmosphere corresponding to the velocity figure. Showing very good correlation with the actual timer events with first burnout at 5.2 seconds, the second malemute ignition starting at 20 seconds and ending at 31.7.

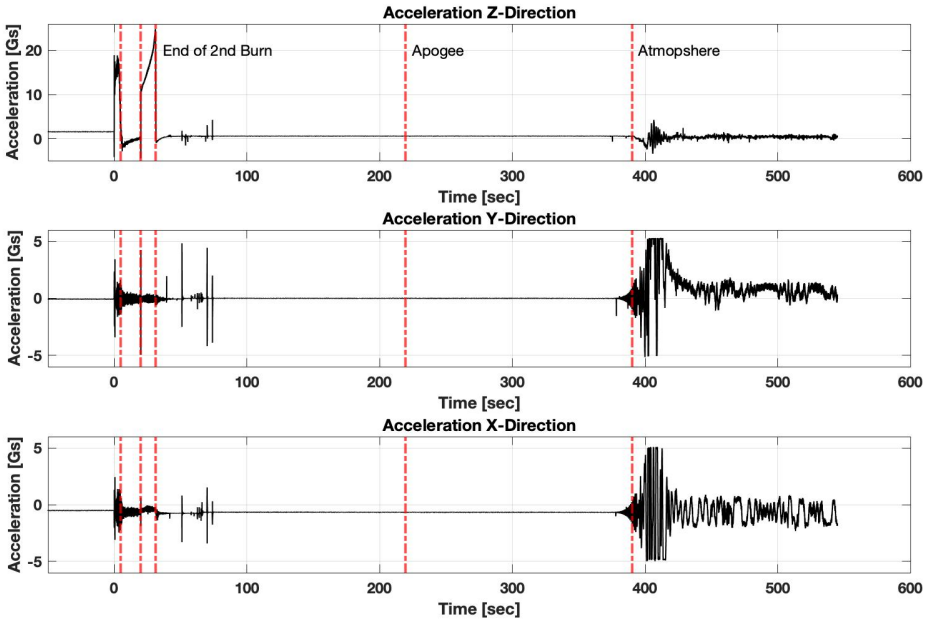

Figure 6.3: Comparison of the acceleration vectors, z, x and y direction. Plot of all the acceleration vectors, z, x and y direction. Marked in red is the end of first burnout, start end end of the seconds burnout, the apogee and when the rocket starts to encounter atmosphere. The data used to plot the figures is provided by NASA Wallops Flight Facility

Figure 6.4 shows the total power to the instrument section on the top deck, which SPID shares with the Japanese team PARM. As can be seen from the figure they had a planned ramp up of power to their instrument at 62 seconds that is marked in the figure. Else the graphs show no indication of malfunction in the total power to the instruments and that all was working nominally.

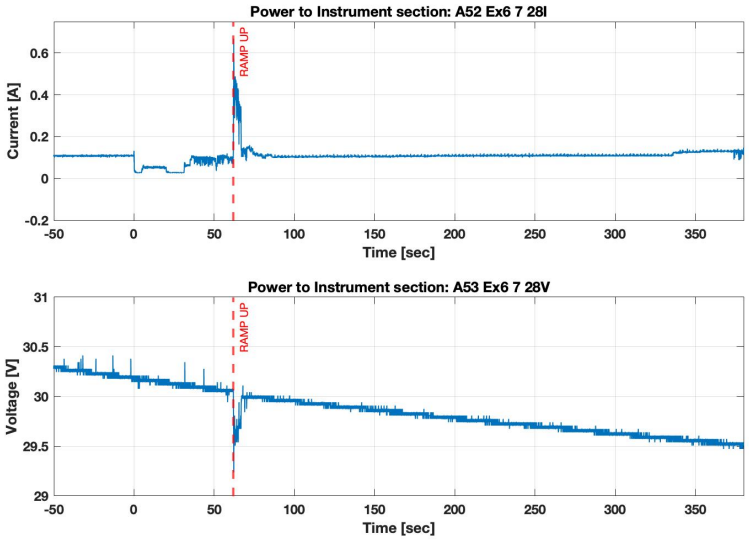

Figure 6.4: Plot fo the power measurements to the instrument section. SPID shares this section with the JAXA/PARM team, their instruemnt had a power ramp up at 62 seconds that is shown in the plot. The data used to plot the figures is provided by NASA Wallops Flight Facility

Figure 6.5 shows the measurements of the magnetometer of the rocket in x, y and z directions. Here the x direction is pointing along the rocket while z and y directions are perpendicular to the flight axis. In all the images the nosecone separation and the de-spin are shown in red. First the nose cone is separated at 51 seconds, this causes a slight shift in the direction of the rocket as can bee seen by the z axis, the de-spin of the rocket is at 66 seconds which can clearly be seen in the data. With the spin frequency going down and the coning of the rocket increases as can bee seen from the z and y axis measurements. The spin frequency and the coning is discussed by Henriette Trollvik in her master thesis and so will not be discussed further here.

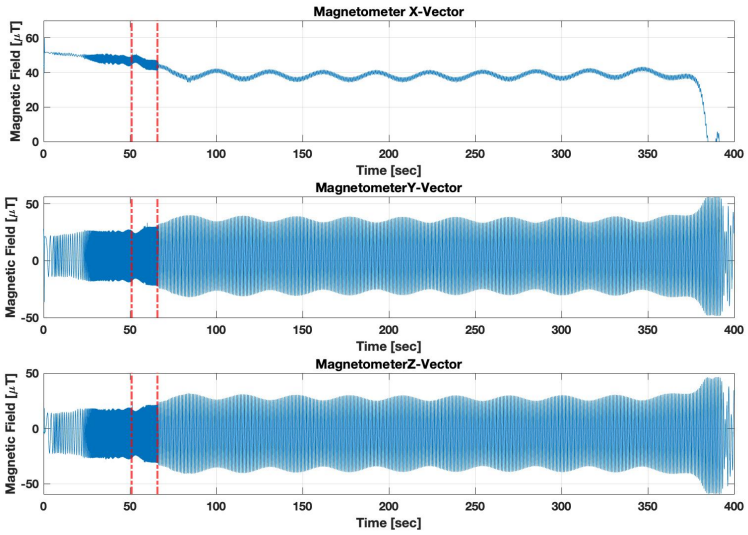

Figure 6.5: Plot of the measurements by the magnetometers on the rocket. Showing the de-spin and nosecone ejection Data from NASA Wallops/Santiago

6.1 SPID Measurements

The SPID measurements are shown in figures 6.6, 6.7 and 6.8, first the raw data collected from all the grids during the rocket flight is shown in figure 6.6, this data is the measured current with time and is not reduced or handled in any way. This shows the saturation of the two first grids, implying that the current measured became to high right after the nosecone separation at 51 seconds.

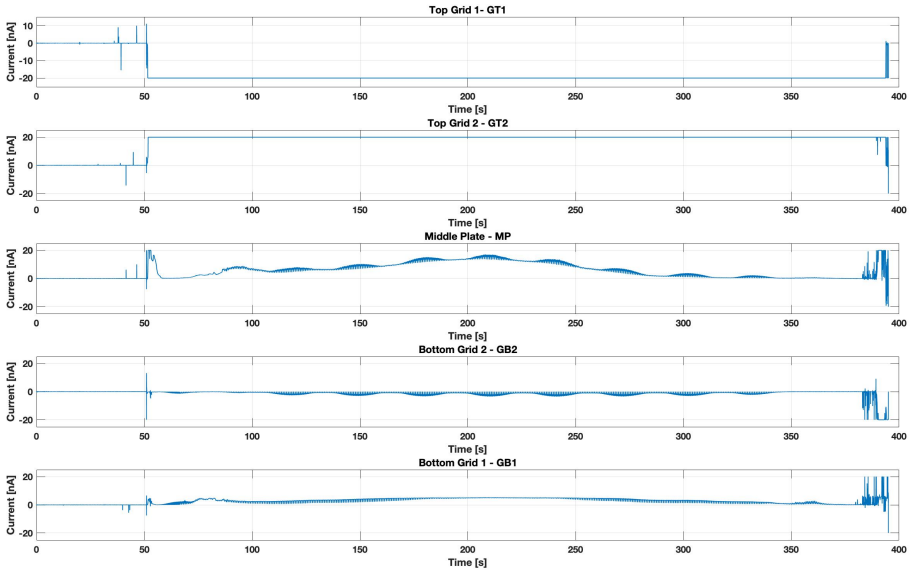

Figure 6.6: Overview of the collected data from all of the grids with time. The top grids can be seen to be saturated soon after the nosecone is ejected.

As can be seen in the below figure 6.7 of the middle plate and the two bottom silver grids is that the signal stays roughly the same on the up-leg and down-leg, this would indicate that the signal id due to ion and electron leakage current or an induced photocurrent by solar photons. These grids show clearly the spin and coning movement at higher altitudes , with the magnitude of the measurements varying immensely in the coning behaviour. This can be due to the movement of the rocket through the wake that forms due to the movement of the rocket through the plasma, causing the leakage current from the plasma to vary as the wake caused the plasma to move slower/faster in areas of the wake, reducing the access of the electrons/ions to the rocket or as will be discussed later the photocurrent.

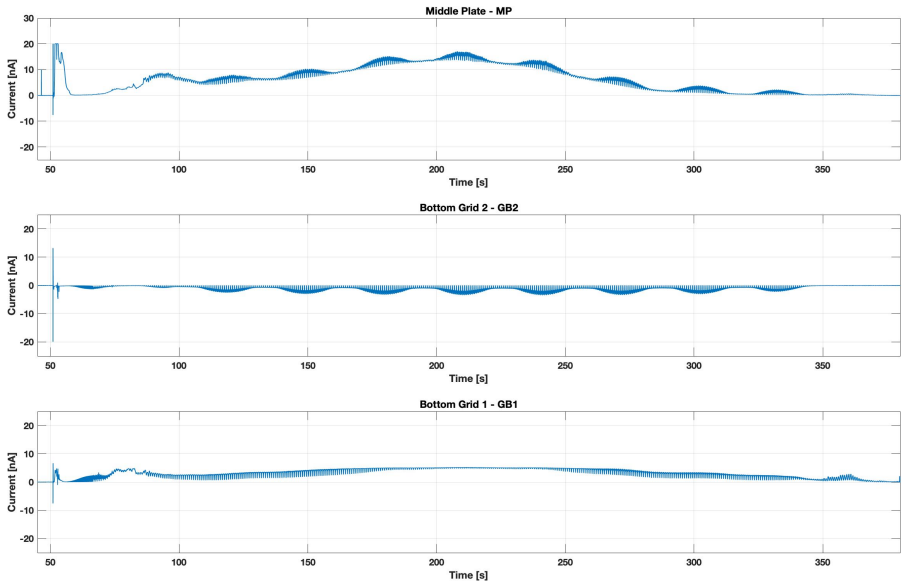

Figure 6.7: Overview of the collected data from the three bottom grids with time. From ejection of the nosecone to atmospheric reentry.

Figure 6.8 shows the current on the middle plate plotted for the up-leg and down-leg separately with altitude. The left plot is the most important since this is where the rocket is pointing upwards. And since it does not have attitude stabilisation it does not measure dust on the down-leg. The most interesting areas of the signal on the left is from 50 to 60 km and from 85 to 100 km. Both these contributions could be due to dust or positive ions(since the to grids are saturated it is possible that they enter the probe and deposit their charge on the middle plate. The signal will be discussed further in subsequent chapters and compared to possible dust current and ion current.

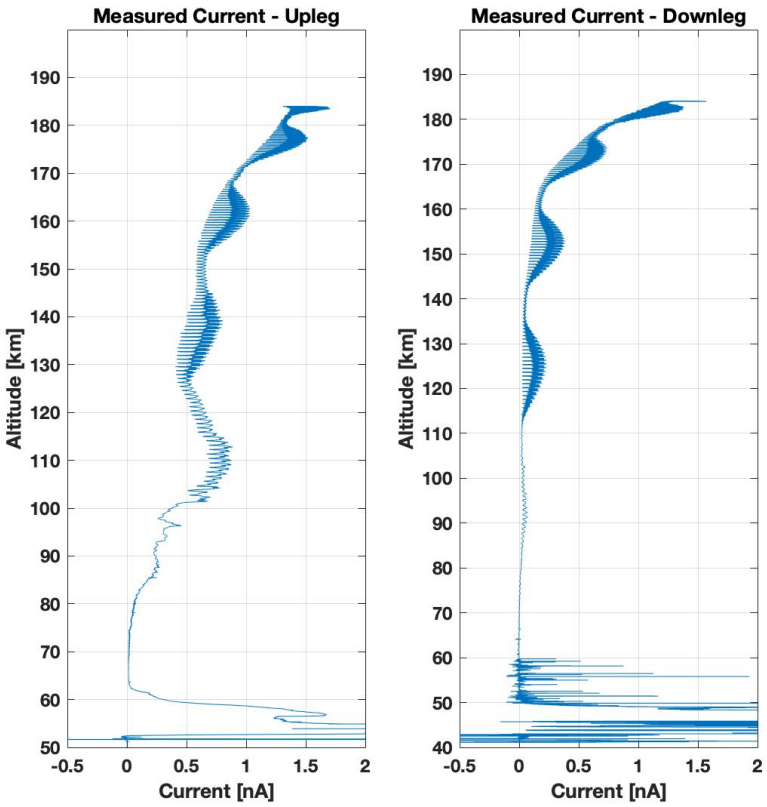

Figure 6.8: Measured current by the middle plate on the up-leg and down-leg of the rocket

Chapter 7

Payload Charging - Results

This section gives an overview of the results of the payload charging from the ambient electrons and ions as well as the charging due to photoemission. In order to calculate the impact of solar photoemission on the payload the solar zenith angle needed to be identified for the time of launch. This gives a good idea of when the rocket was in direct sunlight. Then by using atmospheric data from models the number density and absorption cross sections of molecular oxygen and ozone were obtained, these are important to estimate the optical depth; the attenuation of the solar flux in the atmosphere. The solar flux above the earths atmosphere was gained from satellite measurements onboard SOURCE (of Colorado Boulder, Accessed: 2019-04-01). Then from these considerations the number of photons per wavelength in the UV spectrum were identified and their amount with atmospheric altitude. Then the material properties had to be identified dependent on incident wavelength to ascertain the amount of reflected photons versus absorbed and the photoelectric yield of the material being investigated. This allowed for an estimate of the magnitude of the photocurrent. The photocurrent on the rocket payload was looked at, as well as the possible current generated by direct sunlight on the bottom probe grids - taking into consideration the rotation of the rocket. The payload charging by ambient electrons and ions were considered as well. This is however quite limited since the actual payload potential of the rocket was not measured so a simple magnitude estimate was obtained to gain an idea of the possible payload potential and charge. This was then compared to the photocurrent.

7.0.1 Solar Zenith Angle

The following table has the values used to calculate the solar zenith angle (value also given in the table), the definitions and equations are given in section 4.2.3. The resulting solar zenith angle is over 95 °, this indicated that the sun is below the horizon by more than 5 degrees. This gives a maximum altitude of direct

sunlight of 26.7 km and above.

Table 7.1: Calculated values from section 4.2.3 LSMT is only 15 since the time looked at here is UTC time and not local time

Variable	Designation	Calculated Value
Solar Zenith Angle	θ_Z	95.2410°
Latitude	lat	69.1144°N
Longitude	long	15.7679°E
Hour Angle	ω_H	-40.1935°
Declination Angle	δ	-21.6359°
Local Solar Time	LST	9.3204
Local Time	LT	9.2167
Time Correction Factor	TC	6.2262
Day of Year(DOY)	n	13
Local Standard Time Meridian	LSMT	15
Greenwich Mean Time Difference	ΔT_{GMT}	0
Equation of Time	EoT	3.1546
constant	B	$-1.0386 * 10^3$
Radius of Earth	R	6371 km
Solar Elevation Angle	$90 - \theta Z$	-5.2410°
Minimum Altitude of Direct Sun	z_{min}	26.7764 km

7.0.2 Payload Charging due to photoemission

By following the procedure described in the theory section 4.2 the charging due to solar flux can be estimated. Since the main variation in the solar spectra is the UV range, a proper examination of that spectrum was needed. Several spacecrafts orbit the sun/earth and measure the solar spectrum prior to entering the earths atmosphere, this allows for the spectrum to be estimated before the irradiance is attenuated by atmospheric constituents. Figure 7.1 shows the UV range of the solar spectrum at 13 of January 2019, the launch day of the rocket. This will give the closest picture of the UV part at the top of the atmosphere, and the data comes from the SORCE satellite (SOlar Radiation & Climate Experiment) (of Colorado Boulder, Accessed: 2019-04-01). The top part of the figure shows the data in the range 115-300 nm, the second is the range 115-180 nm, this range includes the Lyman alpha line marked in red on the left side at 121 nm. The last plot has the remaining spectrum of 180 to 300 nm.

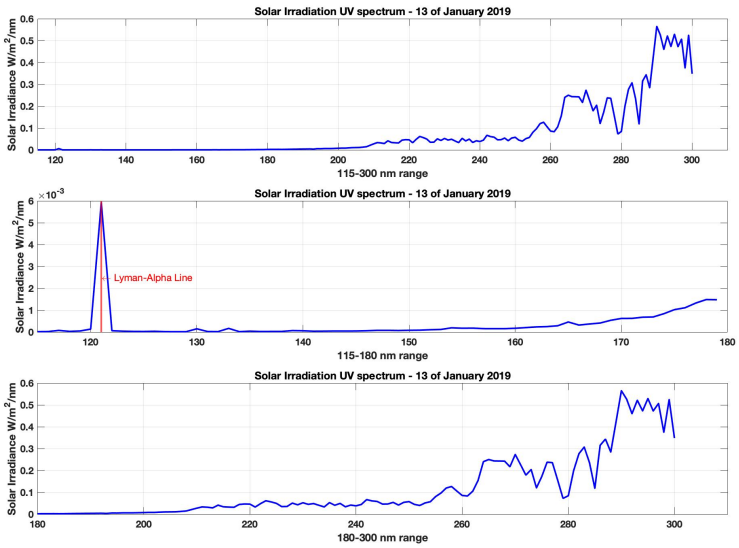

Figure 7.1: Solar Irradiance in the UV part of the spectrum (115-300 nm). Top figure showing the entire UV part of the spectrum, middle part shows the range 115-180 nm, where the sharp peak at 121 nm is the Lyman alpha line - marked in red. The bottom image is the 180-300 nm range. Data from (of Colorado Boulder, Accessed: 2019-04-01)

In order to estimate the amount of direct sunlight hitting the payload the main atmospheric constituents in the range 115-300 nm must be quantified that are the main cause of atmospheric absorption. This includes molecular oxygen O_2 and ozone O_3, and what is needed is their number density with altitude and their absorption cross section per wavelength. Figure a) 7.2 shows the average monthly number density of ozone at altitudes from 0 to 70 km for the years 1979 to 2017 (**?**) From b) 7.2 we can see that by comparing the monthly mean for 38 years, 10 years and 1 year shows not a large difference in the ozone concentration. This data thus does not capture any changes in O3 density with time off day, but can be used for an estimation of the photocurrent. This might give a wrong impression on the total absorption of the UV spectrum at the time of launch. However this database that provides the data have used all the available data to be able to provide an entire map of the ozone concentration, and since the altitude of the ozone is much lower than the main area of interest of the rocket measurement and thus should not matter much.
The number density for molecular oxygen comes from the NRLMSISE-00 Atmosphere Model calculated for the time and day of the launch (CCMC, Accessed:

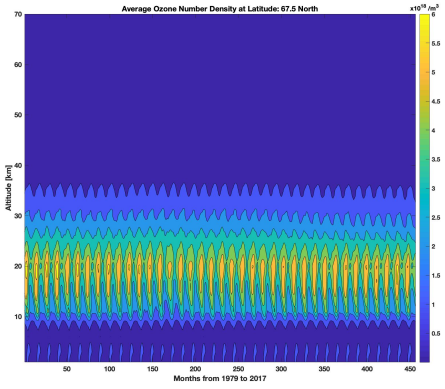

(a) Ozone monthly mean for years 1979 to 2017

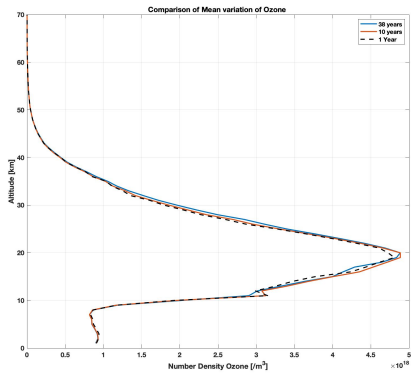

(b) Ozone average Number density comparison

Figure 7.2: Mean values of the Ozone number density for the entire data from the Ozone database and the comparison of the average values (Bodeker et al., 2013)

2019-05-28). Figure 7.3 shows the plotted number density and absorption cross section for molecular oxygen and ozone. Ozone number density chosen from 0-70 km, above 70 km the number density decreases and will not have large effects on the optical depth and the photocurrent. The absorption cross section for molecular oxygen is taken in the range 115-189 nm, while 115-300 nm for ozone. The main rang of absorption is 115-300 nm, however for O_2 the absorption cross section decreases exponentially and is thus not important for the estimate of the photocurrent. The change in the absorption cross section with temperature in the range 150 to 190 nm will not be addressed here.

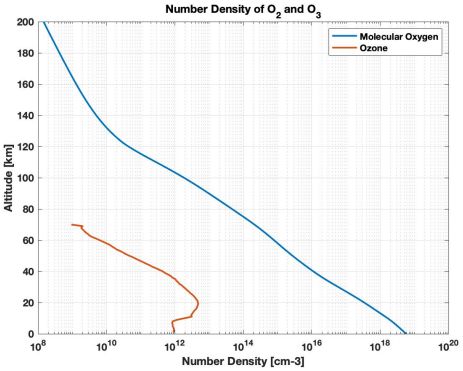

(a) Number density of Molecular Oxygen and Ozone up to an altitude of 200 km. Data from (CCMC, Accessed: 2019-05-28; **?**)

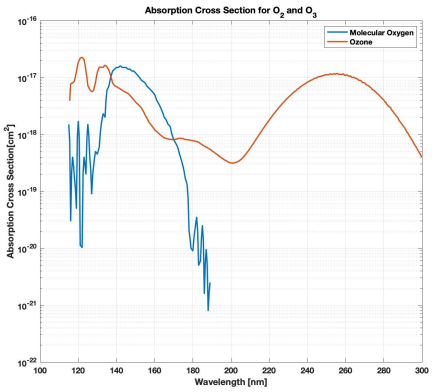

(b) Absorption Cross Section for Molecular Oxygen and Ozone for wavelengths of the UV spectrum; 115-300 nm. (Giono et al., 2018)

Figure 7.3: Number density and absorption cross section of molecular oxygen and ozone for altitudes 0-200 km and wavelengths of 115-300 nm. The absorption cross section of molecular oxygen is only taken up to 189.

Now the optical depth can be calculated using the number density and absorption cross section for both constituents using equation 4.9. Comparison of the results to the absorption cross section shows a link between them. (that sounded weird). The absorption of ozone is much stronger below 70 km and int he entire wavelength range. While molecular oxygen is mainly strong below 190 nm, with a shape much like its cross section from figure 7.3 b). So the optical depth is mainly dependent on the absorption fo the ozone below 70 km and above that the molecular oxygen is dominant with a strong dependence on the absorption cross section for both constituents. Ozone is much more prominent as well in the hight wavelength range. It must be noted that the scale on the figures are not the same, this is done deliberately since that bringing them to the same scale results in any details in the absorption of ozone to be hard to see, the scale for the ozone absorption is from 5 to 8.5 while the scale for molecular oxygen the scale is -6 to 6. So the maximum absorption for ozone is at around 8-8.5 at low altitudes which is to be expected for low altitudes and higher wavelength ranges.

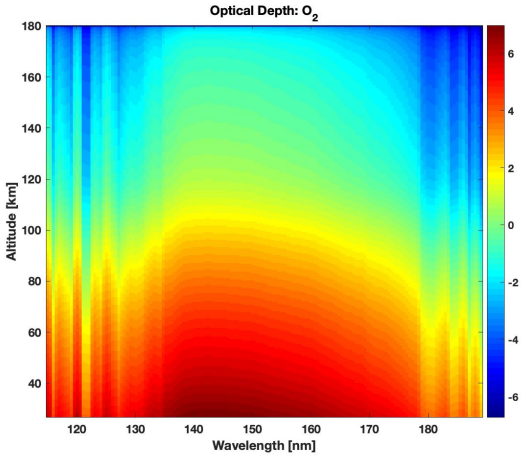

(a) Optical Depth Molecular Oxygen

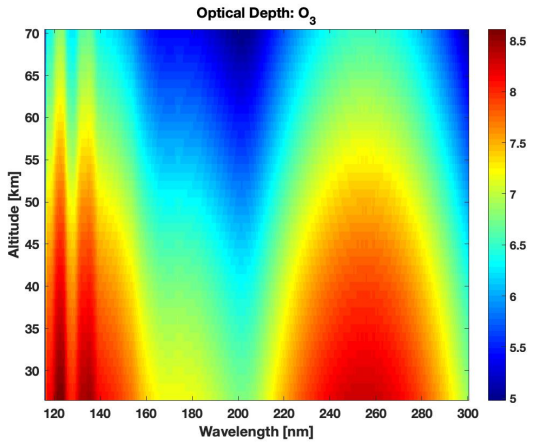

(b) Optical Depth Ozone

Figure 7.4: Note: axis not the same

Now using the optical depth the number of photons at each altitude and for each wavelength range can be calculated. Results shown in figure 7.5,showing the amount of generated photons for several selected altitudes. The photons generated below 75 km are almost zero and the overall magnitude compared to Giono et al. (2018), this is to be expected since the solar zenith angle used here is so hight compared to the solar zenith angle where they used 75 °. The general shape is however similar for the high altitudes which is also to be expected. The Lyman-alpha line at 121 nm is clearly well defined in al the altitudes above 90 km and it dominates the photons generated in the close continuum.

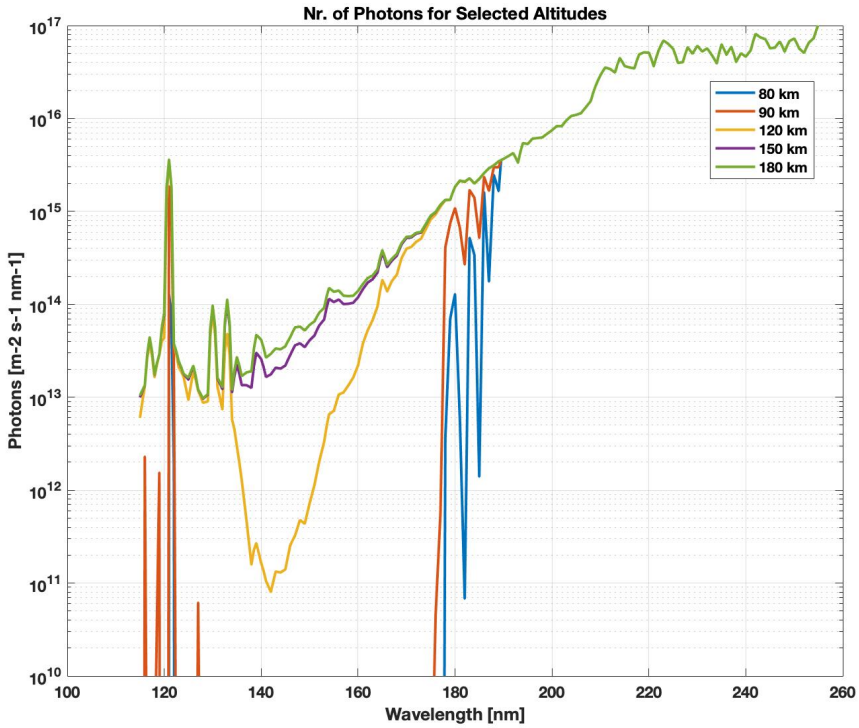

Figure 7.5: Number of photons generated per wavelength for selected altitudes of 80, 90, 120, 150 and 180 km. There are virtually no photons created below 75 km altitude due to the high solar zenith angle and large amount of atmosphere the irradiance has to go through

In order to estimate the amount of current generated per photon with each altitude and wavelength the material properties have to be assessed. The main properties are the photoelectric yield, which gives the probability that a photon can eject an electron in the material as well as the reflectance of the material, which is just the fraction of reflected and absorbed photons, of which the reflected photons will not induce any charge (Giono et al., 2018). To estimate the possible photocurrent of the payload there were several simplification and estimation done. For example the payload was estimated to be a large cylinder, composed of only aluminium. This was done due to the several unknowns, but the estimation should give an accurate estimate of the magnitude of the induced photocurrent. Figure 7.6 below shows the photoelectric yield and the reflectance used for aluminium, stainless steel and silver. These types of metals were chosen to represent the payload section, the middle plate and the silver grids. The photoelectric yield for a material is

the probability that an electron can be ejected for a particular wavelength(Giono et al., 2018). So a high probability means its more likely that an electron will be ejected from the material, in figure 7.6 a) the photoelectric yield is much higher for silver than for aluminium and stainless steel, by two orders of magnitude, and in 7.6 b) the reflectance for each of these materials shows that at wavelengths below 180 nm stainless steel has very hight reflectance(low absorbance) which indicates that much less electrons will be generated at these wavelengths. For both aluminium and stainless steel the data was only available for the wavelengths 115-180 nm, while for silver the reflectance was only available for the higher part of the wavelength range. This however is not a large factor since the photoelectric yield for aluminium and stainless steel are more than two orders of magnitude smaller for wavelengths higher than 200 nm. Thus the probability of ejecting an electron is extremely low, even though the absorption is at a 100 %. It must be noted that the absorption is given and 1- Reflectance and that hight reflectance means low absorption. These values combined with the data given above can now bee combined to give the total photocurrent for an aluminium payload approximated as a cylinder in figure 7.7. Here it is assumed that only the sides of the cylinder in direct sunlight can generate charge, also it is assumed that only a quarter of the payload is in direct sunlight at a given time. This was done to account for the fact that the amount of photocurrent generated is highest at 0 degrees incidence and almost zero at 90 degrees incidence angle, and since the payload is assumed a cylinder the effective area in sun at a given time will be roughly a quarter of the total surface area of a cylinder. And since this is to gain an understanding of the possible magnitude of the current the estimation seems to be valid enough.

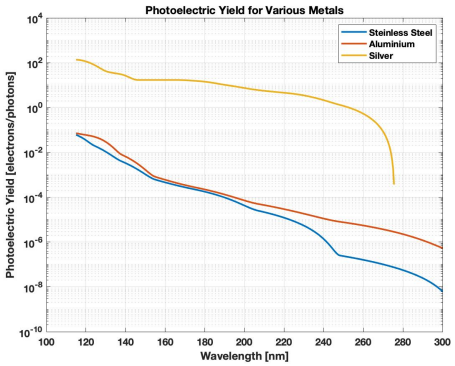

(a) Photoelectric yield for silver, aluminium and stainless steel

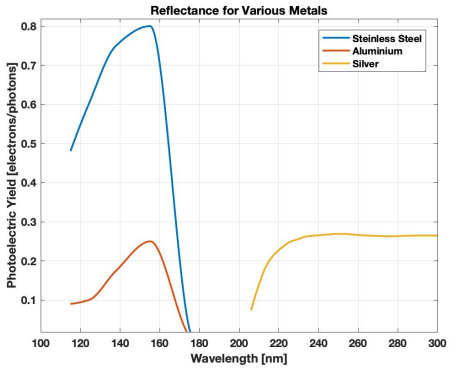

(b) Reflectance for silver, aluminium and stainless steel.

Figure 7.6: Material properties for the metals that are considered; the photoelectric yield and the reflectance for the wavelength ranges of 115 to 300 nm(Giono et al., 2018)

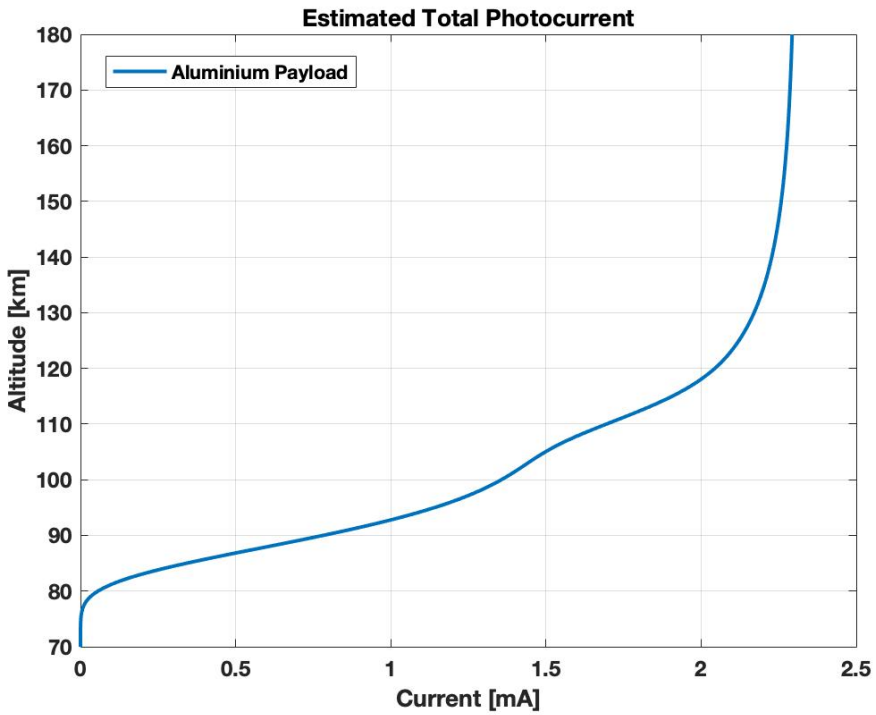

Figure 7.7: The estimated photocurrent for an aluminium cylinder at altitudes 70 to 180 km are shown. The current below 70 km is so small it is essentially zero. Possible photocurrent with a maximum current of about 0.45 mA

Using the photoelectric yield for stainless steel the photocurrent due to incident sun on the middle plate can be calculated. Since the plate is thick and has concentric rings, its area can be considered equal to the probe inner diameter and it can be approximated as a uniform slap of steel. The resulting current can then be compared to the measured current on the middle plate with the maximum current given in figure 7.8 is if the plate was constantly in the sun throughout out the flight. This is then compared to 1, 5, and 10 % of that maximum current, since the rocket is both rotating and coning there will be different opportunities for a direct sun the entire altitude range. In general the 5 % current follows the general magnitude of the measured middle plate current. It is however more likely that a current between 1-5 % is the correct one for altitudes above 100 km and it is quite possible the result of the increase in the current that shows clear signs of spin and coning effects above this altitude. This is not visible in the signal at lower altitudes, this might be due the fact that it's not until above around 25 km that the payload is in direct sun and up to around 70 km the absorption of ozone is very high due to the low solar zenith angle. SO above 80 km there is a better

change of direct sun onto the grid and not scattered likely below. The argument that the increase in magnitude in the signal at higher altitudes is also very similar on the up-leg and down-leg of the rocket path as was seen in figure 6.8 where the increase in the signal reaches a constant magnitude and is the same going up and down. This can be better analysed by doing an accurate ray tracing analysis of the times the probe is in direct sunlight as well as the illumination of the middle plate.

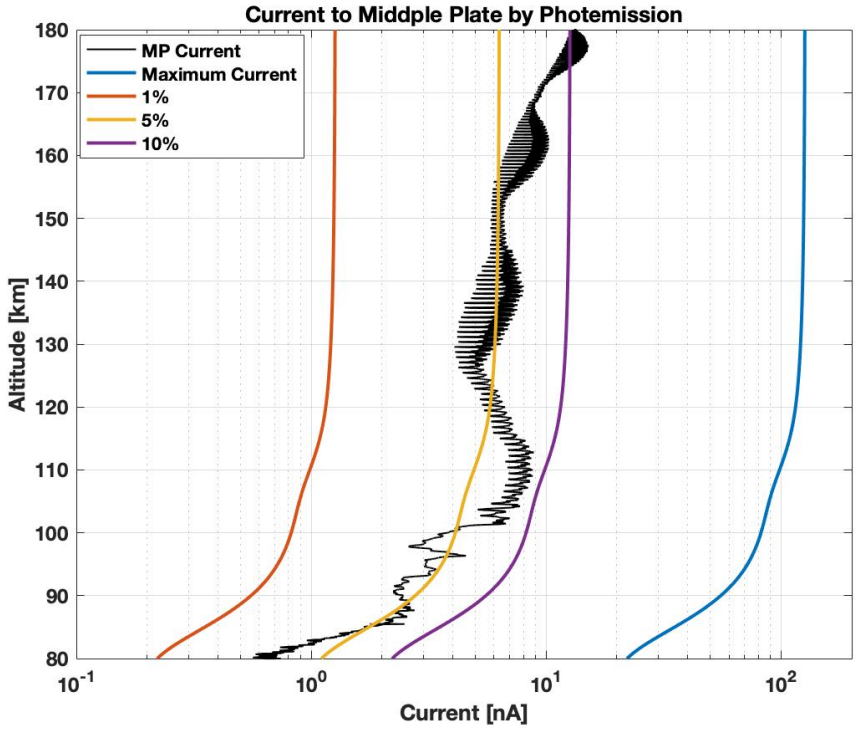

Figure 7.8: Comparison of the measured signal from the middle plate to the possible photocurrent generated for different magnitudes in direct sun. With 100 % the plate is always in the sun

Comparison of the photocurrent generated on a silver grid withe the measured current on the negatively biased grid GB1 is shown in figure 7.9. Showing large discrepancies between the measured current and 1% of the grid being in constant sun. This is most likely due to the photoelectric yield being way too high for a grid that is made of silver coated brass, while the photoelectric yield chosen to model the possible photocurrent was for pure silver. It is also possible that the grids are never in direct sunlight and thus the current is not affected by this.

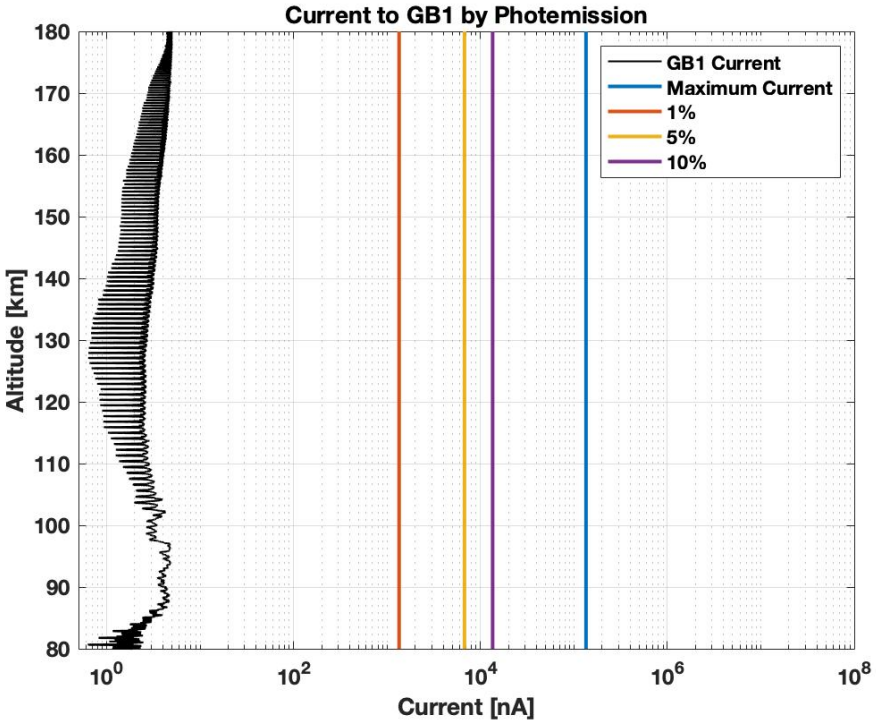

Figure 7.9: Comparison of the measured signal from the negatively biased (-10V) GB1 grid at the bottom of the probe to the possible photocurrent generated for different magnitudes in direct sun. With 100 % the plate is always in the sun

7.0.3 Charging due to ambient plasma

To evaluate the amount of charging due to ambient plasma on the rocket the procedure in chapter 4 is followed. The main problem in estimating the current of electrons and ions to the rocket is that these currents depend on a somewhat accurate measurements of the payload potential. This was not measured on the G-Chaser rocket and can thus only be estimated. This however remains enough for the current study, since an order of magnitude current contribution is good enough to give a general idea of the possible magnitude. In order to estimate a possible current the data measured by EISCAT at the time of launch of the electron density and electron and ion temperature were used. Available data was for both the UHF and the VHF EISCAT radars, however due to less altitude resolution and high variations in the UHF data, the VHF measurements are used for this analysis. To maintain quasi-neutrality it is assumed that the electron and ion density are equal for and for altitudes over 70 km. As can be seen from figure 7.10 that shows

the altitude of the rocket and the different regions of the ionosphere are shown

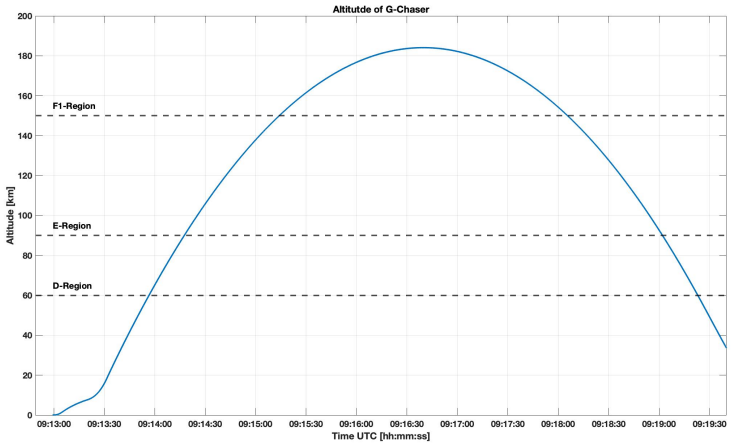

Figure 7.10: Altitude of the rocket with different layers of the ionopshere

Figure 7.11 shows the average electron number density, electron temperature and ion temperature. The average is taken over all the measurements at each altitude at the duration of the launch(around 500 seconds). This is done since we are only interested in the estimate of the total current to the rocket and an average value of the measurements is good enough for that purpose. The electron density shows in general a linear increase in the density.

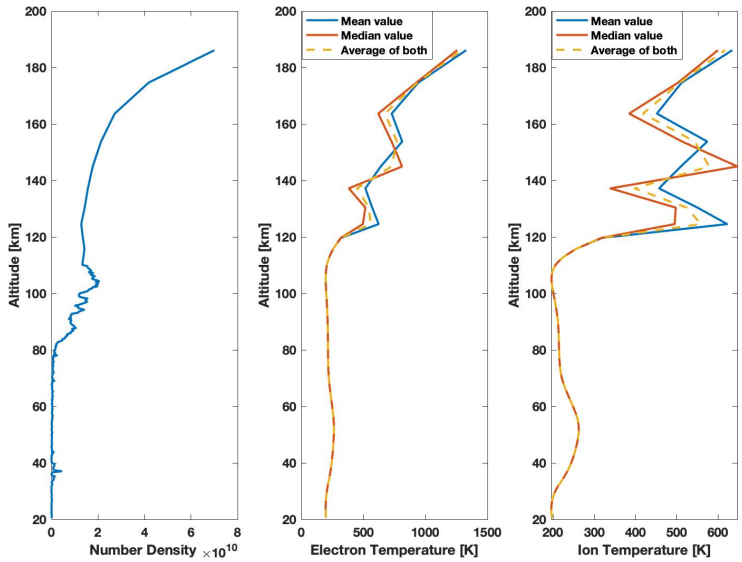

Figure 7.11: Measurements from the VHF EISCAT radar taken at the time of launch. With Electron density and electron and ion temperature averages. The dashed yellow line for both temperatures is used in estimations of the current contributions.Time used for the generation of the plot is from 9:13-9:18 UTC

Comparing the average electron thermal velocity (equation 4.5) to the rocket velocity shows that the rocket is essentially not moving compared to the high velocity electrons as can be seen in figure 7.12, the thermal velocity is on average two orders of magnitude larger than the rocket velocity. This means in practice that the electron have access to the entire surface area of the rocket, where this surface area is estimated to be the surface area of a cylinder with the same radius and height as the payload section. Since the ions have much lower thermal velocity they are estimated to only affect the charging of the rocket in the ram direction(Darian et al., 2017). To account for a possibly larger contact area due to coning of the rocket the double area of the top of the cylinder is used to calculate the ion current.

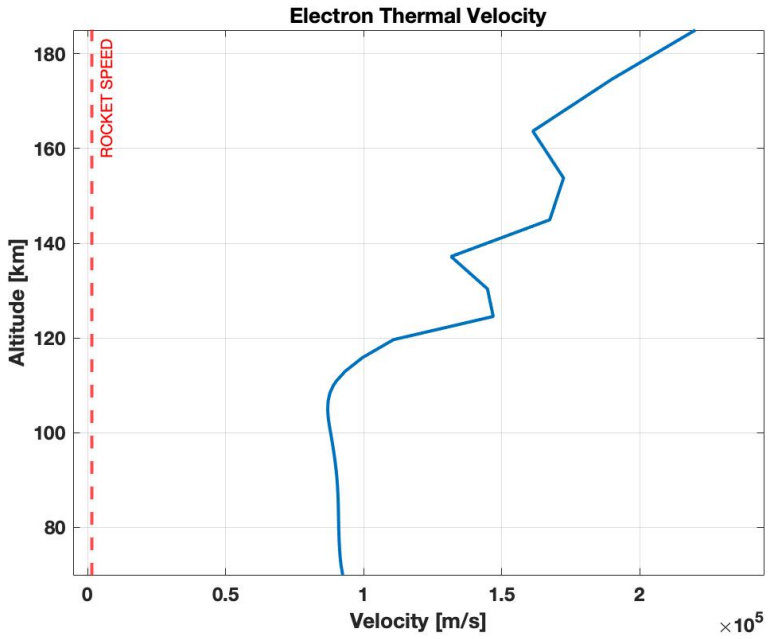

Figure 7.12: Electron Thermal Velocity compared to the rocket velocity set as 1500 m/s.

Now by calculating the current from the electrons using equation 4.4 and the contribution form the ions current using equation 4.2 we can see the total current from the ambient plasma given below in figure 7.13. The payload floating potential gives a rough estimate of the variation in the rocket potential. With a maximum value of around -0.45 V at apogee as can be seen in the figure, which is reasonable and comparable to potentials on other rocket flights. The estimated electron current is shown to reach a negative value of around -2.5 mA at 80 km and up to -15 mA at apogee which is reasonable. The ion current is more than two orders of magnitude lower than the electron current and can in turn be neglected when estimating the total charging of the payload since the electron current is so much larger.

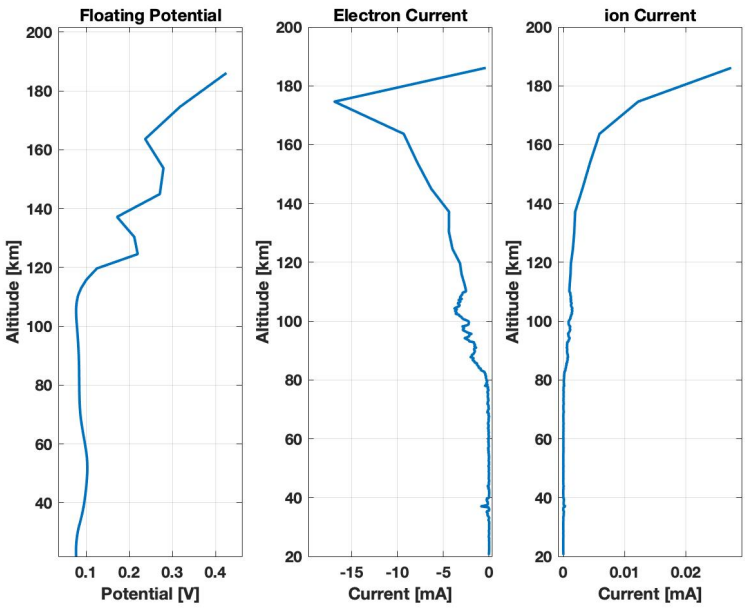

Figure 7.13: Estimate of the payload potential, electron and ion currents with altitude. Calculations form equations 4.2, 4.4

7.0.4 Total charge on payload section

Now the results from the calculated current from the ambient plasma and the photocurrent can be compared and the total current to the rocket with altitude is examined. Figure 7.14 shows the electron current contribution, the ion current and the photocurrent, as was mentioned before the ion current can be neglected in the total current. The maximum contribution from the photocurrent is around 0.45 mA for altitudes above 120 km. So the photocurrent contribution is an order of magnitude lower in general through out the flight and does not lower the total current to the rocket in a significant manner. And since this is just an estimate of the total current to the rocket the electron contribution is the most dominant one. To be able to accurately look at the charging of a payload, the payload potential needs to be measured. This is something to consider for future flights. This would give a much better representation of the payload charging and the negative potential on the rocket since this might influence the measurements as the grids are biased to a pre set potential to the rocket ground, which in turn is changed as the floating potential of the rocket increases.

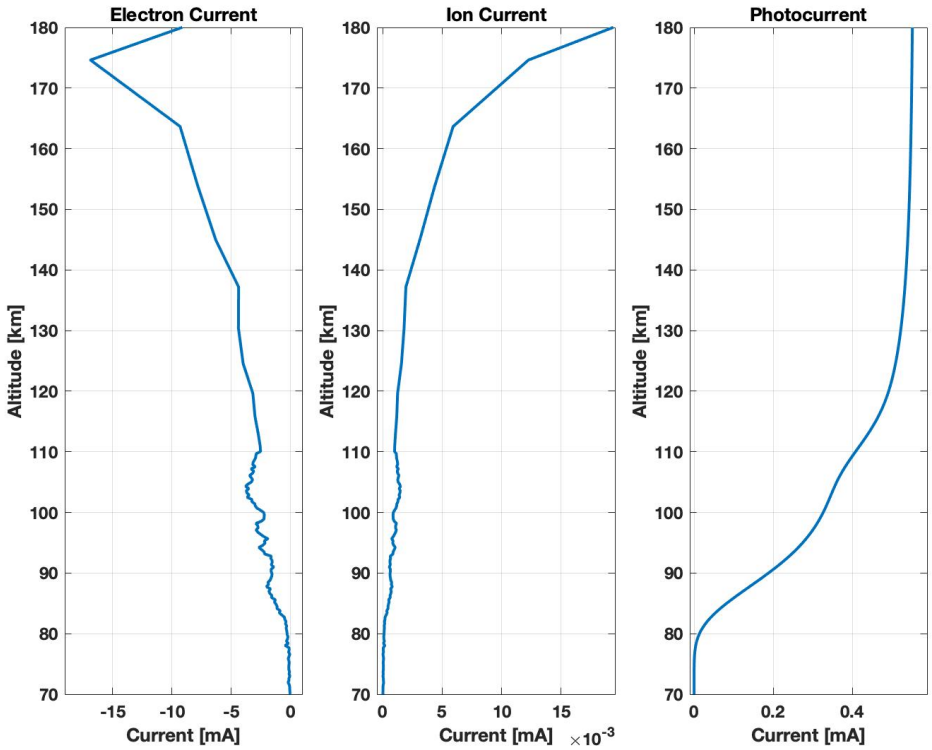

Figure 7.14: Comparison of the calculated total current to the payload, with the electron current on the left, the ion current in the middle and the photocurrent on the right

Now the payload current can be compared to the charging of the grids, in figure 7.15 the current measured on GB1 grid (which is the grid with negative 10 V potential has a measured positive current due to positive particles through the probe, in the middle plot is the current generated for the number density of ions considering the total flow flow rate through the rocket and collision efficiency of 50 % , this is then compared to the plot on the right which is the ion current contribution in the ram direction of the rocket calculated previously with equation 4.2, Since the plot in the middle and on the right are proportional to the density they retain the form of the electron and ion density, which has been assumed to be about the same due to quasi-neutrality. From a general comparison standpoint there are some similarities between the GB1 grid and the plotted ion current, two peaks in the data from 90 to 95 km are seen in both currents as well as the current measured at 85 km, indicating that the grid is measuring an ion contribution in the area from 85 to 95 km altitude. Above 95 km the currents are not as similar,

with some peaks in the measured data at around 105 km, indicating that the ions being measured are possibly not entering the probe as efficiently as in the altitude region below. The general form however of the measured current above 110 km are very similar to EISCAT current, ignoring the contribution of the spin effects. The discrepancies in the two plots are mainly at altitudes of up to around 85 km, with a larger contribution in the measured current, this can be either due to positive particles other than ions interacting with he grid or the fact that EISCAT is not as accurate below 80/70 km Comparing these plots then to the one on the right shows that the form is generally similar, the current is much higher, but this is accounting for all the ions in the ram direction of the rocket, which is the double surface area of the top deck to account for the rocket coning, this area is much larger than the SPID opening surface area and does not account for any charging probability.

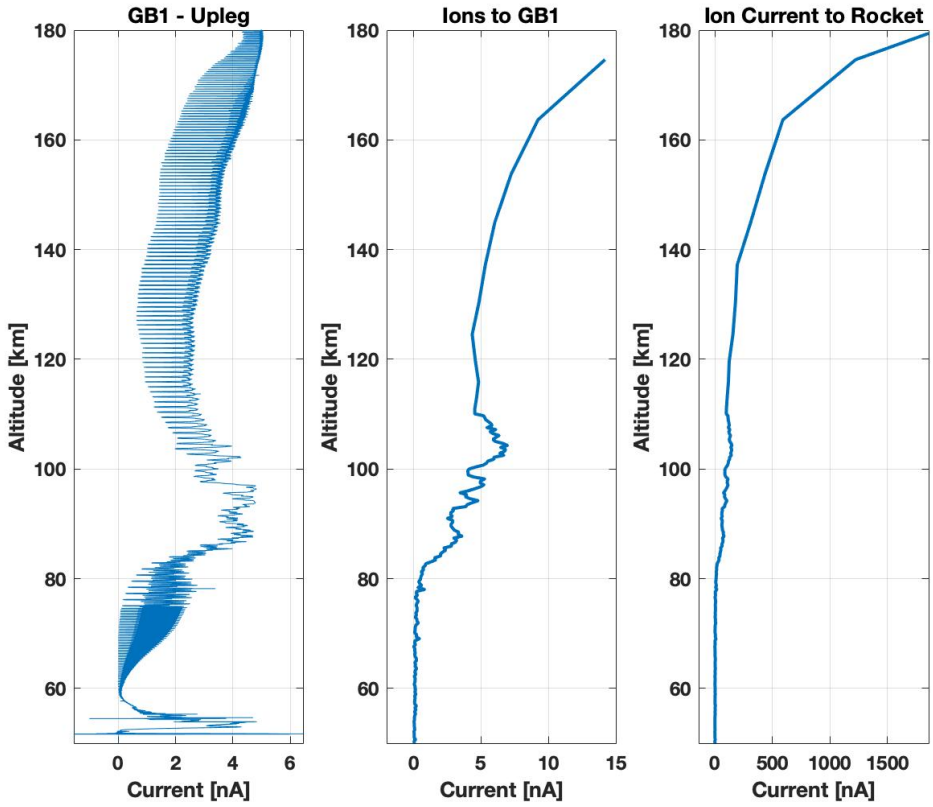

Figure 7.15: Comparison the payload charge, possible ion current inside the probe and the ion current in the ram direction.

Comparison of the measured current from GB2 grid (the second grid from the bottom) and the possible electron current calculated to enter the probe without any potential on the probe and the electron current calculated earlier from equation 4.4 that shows the total electron contribution to the entire payload. Even though the magnitude of the compared currents in figure 7.16 are very different the magnitude difference can be explained from the fact that the current on the far right is the contribution from electrons hitting the payload from every direction, compared to the middle figure, which is just the current generated from electron to an area the size o the probe opening is considered. As can bee seen from comparing them all together is that the negative current on the GB2 grid ,at altitudes from 60 to around 100 km, cannot be from electrons entering the the probe (that have not collided or been deflected by the previous grids). The current above 100 km have a roughly similar shape except for the large coning visible in the current at higher altitudes. This large coning is hard to explain since the rocket is essentially not moving according to the thermal velocity of the electrons, that also increase with higher altitude. There is also no negatively charged dust coming from the middle plate at this high altitude. What is odd is the current measured at altitudes around 90 to 100 km, where it is close to zero. Here we should expect a possible current from negatively charged particles that might collide with the GB2 grid as they exit the middle plate area. This is assuming that the particles have managed to gain a negative charge by interacting with the middle plate. The current on the GB2 is more likely to be a result of electron leakage current or by photoemission from the sun.

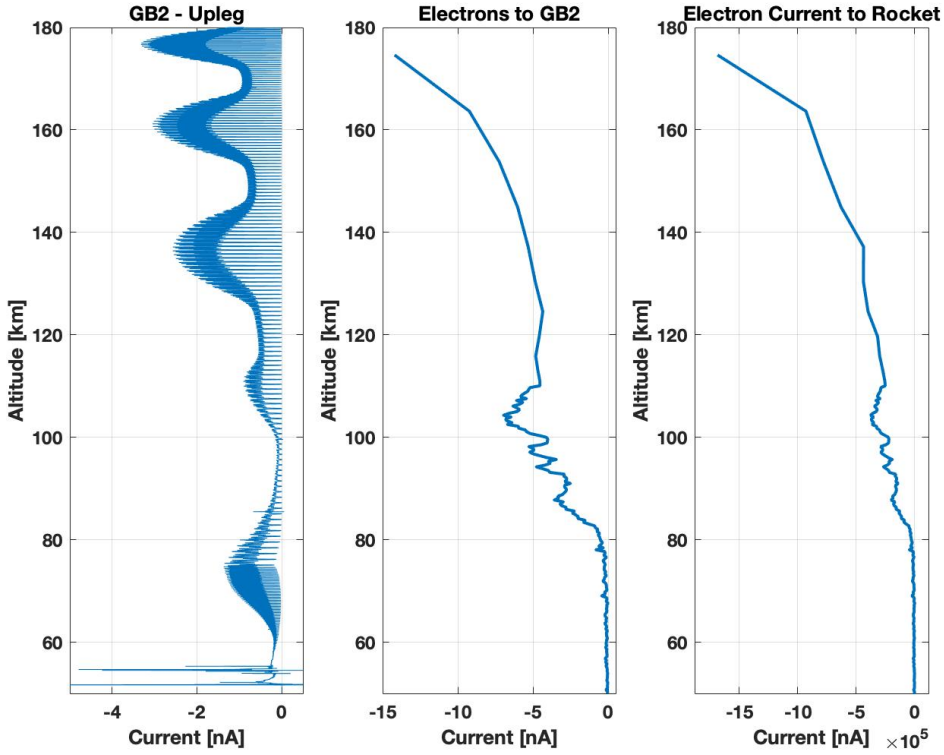

Figure 7.16: Comparison the payload charge, possible ion current inside the probe and the ion current in the ram direction.

By comparing the current of the middle plate in figure 7.17and the possible current due to ions inside the probe shows that ions contribute considerably to the middle plate current int he altitude region above 80 km. EISCAT has not measured nay number density of electrons and ions below 80 km and is in general not reliable below that altitude. The main result from comparing these two images is the large current contribution from 50 to 60 km. Here the current is large and seems to measure a layer of positive or neutral particles. Whether this current is due to a smoke particle layer at this altitude or a result of the nosecone opening can be debated. The nose cone is opened at 50 km and the measurements from the middle plate are instantly saturated. Then the current starts to go down, but clearly is influenced by something after that and there is an increase in current again, then it goes all the way down to zero again. The current measured is more than 15 nA and is quite high. By comparing this with the theory of triboelectric charging and the amount of charge that could be possible, in the following chapter.

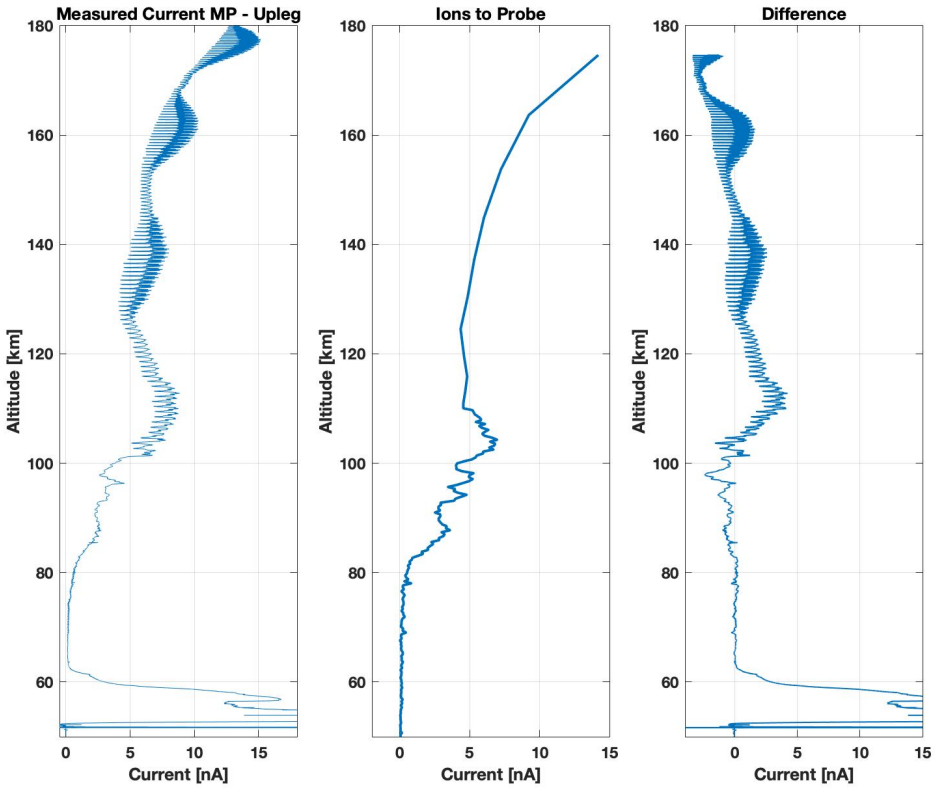

Figure 7.17: Current measured on the middle plate compared to the possible current due to ions and the difference between these two currents

Chapter 8

Charge of Particles inside the probe - results

To base the several possible charging models for the collision of the particles with the middle plate it is necessary to have some idea of the possible size, composition, material properties, work function, number density and altitude distribution. This is not as simple since these remain mostly unknown for MSPs, but a combination of models and previous rocket experiments can be of some assistance in estimating these values or at least using values for similar materials. The number density, size and altitude distribution used in the calculations bis taken from the model run by (Baumann et al., 2015) that is based on simulations done by (Megner et al., 2006), this data is shown below in figure 2.3, this is for a model run for 8 of September 2010 and is run for 24 hours. Since the rocket is launched in December at 9:13 UTC the number density and size distribution will most likely be different but it gives an indication of the current generated by the particles for these kind of conditions. The conditions at 3:30 local time from the model were chosen by me and Henriette Trollvik, this time was chosen for the conditions to most likely match out conditions in December. This decision was based on the solar elevation angle to be 5 degrees below the horizon at both times, the launch time(as has been mentioned previously) and the model time at 3:30. The model assumes negative, positive and neutral concentrations of dust in 11 size bins. These 11 sizes are the average size for each size bin as is seen in figure 2.3. An overview of the total number density of electrons, ions and MSPs are given in figure 8.1. Table 8.1 gives an overview of the material properties for several different metal particles as well as stainless steel (middle plate material) that will be used in calculations for the coming sections.

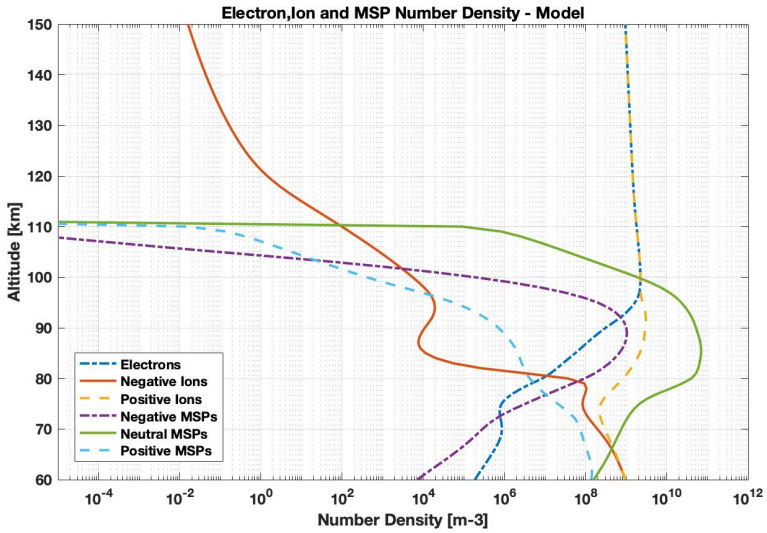

Figure 8.1: Number Density of electrons, ions and MSPs from altitudes of 60 to 150 km. Data from model by (Megner et al., 2006) and prepared by (Baumann et al., 2015)

Table 8.1: Table over various material properties for metal particles considered in the following sections(Rennecke and Weber, 2014; Rapp et al., 2012; Aksteel, Accessed: 2019-05-20; ToolBox, Accessed: 2017-12-1; Inc., Accessed: 2019-04-01).

Metals/ MSPs	**Work Function** [eV]	**Density** [g/cm3]	**Poisson's Ratio**	**Young's Modulus** [GPa]
MSPs	4-4.6	2-3		
Fe	4.67		0.21	210
Mg	3.66		0.35	45
Si	4.6		0.22	165
Al	4.2		0.33	69
Ag	4.5		0.37	73
Ag	4.7	10.5	0.37	104
Au	4.8	19.3	0.42	171
Stainless Steel	4.3-4.4	7.99	0.29	193

8.1 Maximum Charge on Nanoparticles

First the maximum charge a nanoparticle can have needs to be examined. This is done by comparing the limit for which a particle will emit an electron, given in equation 5.21. This sets an upper limit on the maximum negative charge a particle can gain before starting to emit excess charge. This limit is compared to the particle disintegration limit. Meaning that a particle will disintegrate due to too large forces of opposing electrons, ripping apart the particles(Mann et al., 2014). This limit is given in equation 5.22. Figure 8.2 shows the two limits compared per size of the particles The blue lines represent the electrostatic disruption limit per particle size with different values of γ varying from $1e-4$ to 1, these values depend on the material properties as was discussed in section 5.3. The dashed black line represents the electron field emission limit per particle size, representing the limit of amount of charge that can occupy a small particle without emitting electron from the material due to the electron field being too strong to keep the electron on its surface(Mann et al., 2014). The red lines added in the graph are number of electron charges, with -1, -20 and -200 charges. showing that for γ values below 0.1 the disruption limit dominates the maximum charge allowed on a particle for all sizes up to 5 nm. For larger γ values the the electron emission limit will dominate except for particles smaller than 075 nm for γ value of 0.1. For γ value of 1 the electron emission limit. As was discussed in section 5.3 the assumed value of γ for MSPs is chosen as 1, since that limit is set by volcanic rock and closely resembles the process of meteor ablation and condensation/coagulation. That means that if that is valid for MSPs the electron emission limit dominates the charging process for all sizes of MSPs and sets an upper limit on amount of charge for nanometer sized particles.

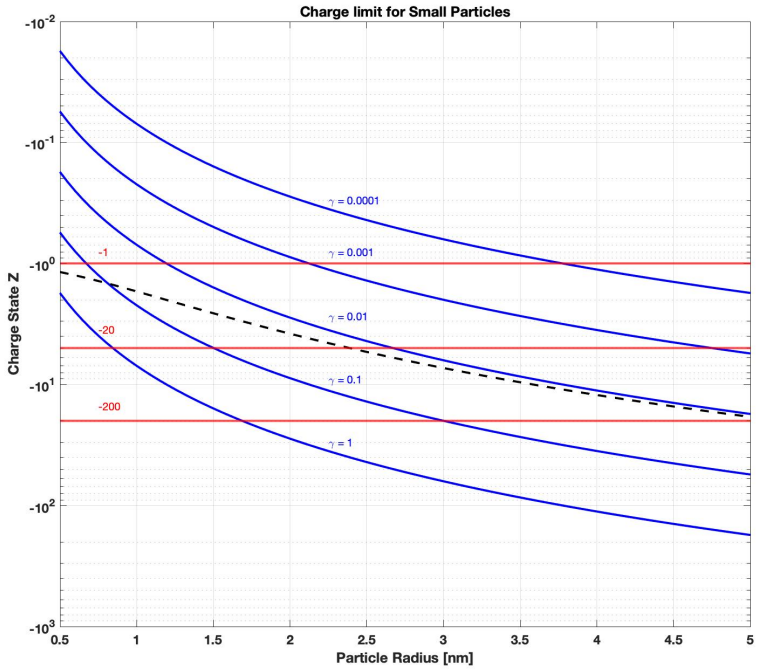

Figure 8.2: Charge limit for small particles, taking into account electron emission and disintegration of particles

8.2 Charging Models

By testing and comparing the different charging models previously discussed we gain an understanding of the amount of charge particles in the nanometer range can gain by triboelectric charging interaction with the middle plate. As is similar for all the charging models mentioned is that they have been tested against laboratory experiments often for much larger particles, both micro meter sized particles a well as some nanometer sized particles of sizes 20-100 nm. Since the assumed size distribution of the MSPs has a large amount of particles in the size range lower than 5 nm this creates a problem in relating the theories with smaller size.First the different charging models are compared to each other and the number of charges per particle radius is plotted in figure 8.3 for no bias on the middle plate. The largest variation in the models can be seen for the small particle limit. The only model that predicts any charge for particle sizes below 1 nm is by Wang and John (1988), this model however also goes above the electron emission limit discussed earlier. Above that limit the particle will emit any excess charge it gains. The

other models however stay under this limit in the size range depicted. The plot for John (1995) and Matsusaka et al. (2010) are almost identical, with a slightly higher charge for the latter model. These two models set a lower limit for charge generation at little below 2 nm, meaning that no particles below that radius would generate any charge. The model by Adams and Smith (1971) shows no charge production for particles below 2.5 nm. This low charge production is clearly due to the small difference in work function for the particles chosen. Here the particles used for the models are iron particles. Except for the Adams and Smith (1971) model which does not include/depend on particle properties. Now in figure 8.4 the bias on the middle plate is included in the calculations. This means that the effective work function of the middle plate is 6.3 eV instead of 4.3 eV for no biased plate. The number of charges per particle radius is clearly much higher than for the no biased plate, with particles down to 0.6 nm gaining at least one electron in a collision from the Wang and John (1988) model. The models by John (1995) and Matsusaka et al. (2010) predict at least one charge for particles larger than 0.75 nm and for particles larger than 1nm the electron emission limit dominates. Since the model by Adams and Smith (1971) does not depend on the work function or particle properties the number of electrons per particle size remains the same as for a no biased middle plate. It however remains unclear if a particle is gaining more charge than the emission limit if the charging will effectively stop and the flowing current will stop due to the limit or if the particle will gain electron until the limit is reached and then emit the extra electrons where the field emission is strongest. This might indicate that the particles could effectively generate more charge than the limit but emit them through the largest local field on the particle and the escaped electron will then move away from the middle plate due to both high airflow and electric field from the biased middle plate. This effect would need to be further researched/experimented to determine this.

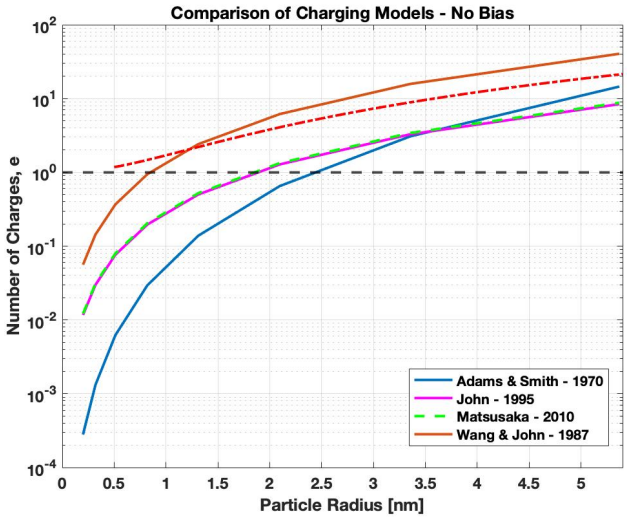

Figure 8.3: Comparison of charging models from Adams and Smith (1971), John (1995) , Matsusaka et al. (2010) and Wang and John (1988). The number of charges, e, are plotted for each respecting charging model per particle size. The bias on the middle plate is set to zero. The dot-dashed line indicated the electron emission limit and the black dashed line represents one electron charge.

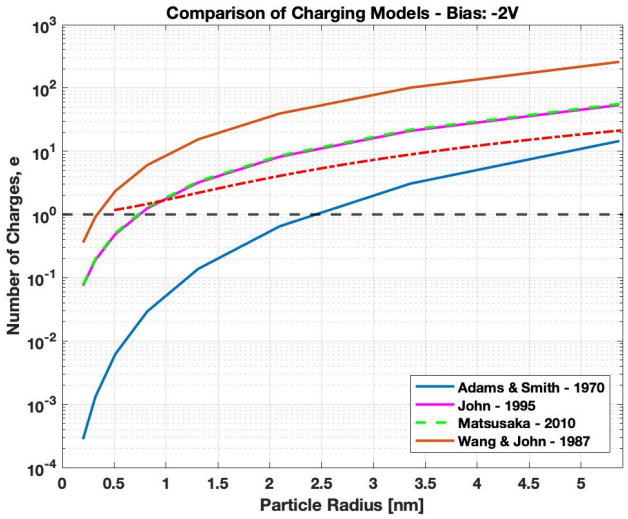

Figure 8.4: Comparison of charging models from Adams and Smith (1971), John (1995) , Matsusaka et al. (2010) and Wang and John (1988).The number of charges, e, are plotted for each respecting charging model per particle size. The bias on the middle plate is set to -2 V as on SPID.

8.3 Varying Model Parameters

Since the charging models by John (1995) and Matsusaka et al. (2010) compare so well I have chosen to look closely at the charging model by John (1995) and the resulting current when the varying the particle density the separation distance between the particles and the surface. AS well as the charge generated by varying the particle impact speed as well as the resulting current for different metal particles with different work function on a biased and unbiased middle plate.

8.3.1 Work Function Dependence

The main idea behind the charge transfer of two metals in contact is that their work function is different and this results in charge transfer between them. As has been shown above the charge generated increases when the bias on the middle plate is included since its effective work function is lower than the impacting particles. There are several mentions in the literature that state that the work function both increases and decreases for small particles. This will however not be considered here. As was shown before, varying the bias on the middle plate effectively changes the potential difference between the metal particles and the middle plate. Figure

8.5 shows the number of charges generated for several different types of metals using values from table 8.1. The middle plate has no bias here which results in a much lower difference between the work functions of the metals and the middle plate and some metals generate positive charge while others generate negative charge. The current generated by the magnesium particles follows the electron emission limit. If the work function of MSPs is in the range 4-4.6 eV and the middle plate would remain at 4.3 eV there would be both a negative and positive current contribution. This would result in a signal from particle both stealing electrons and gaining electrons making data analysis very difficult. By keeping the middle plate at a bias as in figure 8.6 all the current contribution from the metal particles have the same sign with slight variation in the magnitude of the number of charges possible for different metals. This difference depending on the respective work functions and the mechanical properties of the particles; the young's modulus and the Poisson's ratio(see table 8.1 for numbers used). It is worth mentioning that the work function and young's modulus are dependent on temperature, and increase with increasing temperature. This effect is not considered here since the temperature of the middle plate is not measured during the rocket flight, while the temperature of the MSPs can be gained from neutral particle simulations(Henriette Trollvik's master thesis can be consulted for neutral airflow simulation including temperature of the neutral airflow).

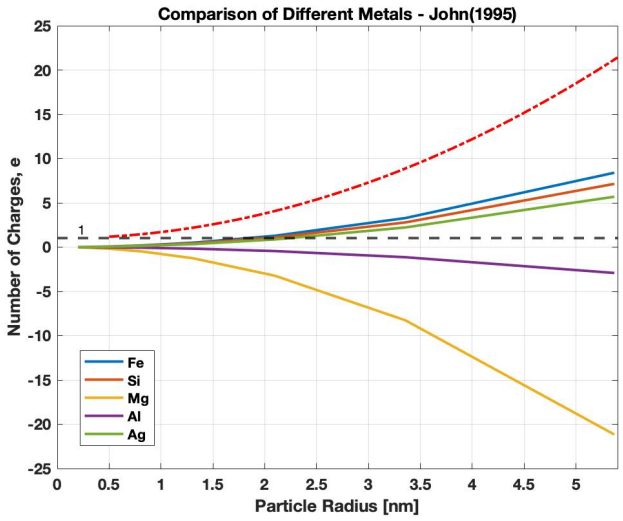

Figure 8.5: Number of charges produced per particle radius for different metal particles with no bias on the middle plate. Using charging model by John (1995).The black dashed line represent one electron charge limit and the red dot-dashed line represents the electron emission limit.

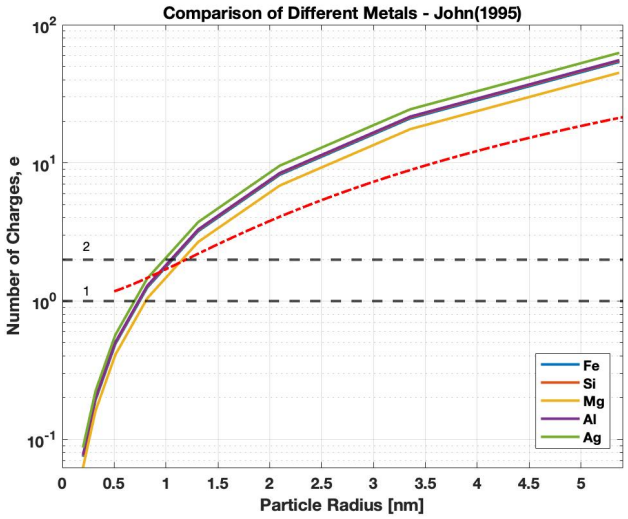

Figure 8.6: Number of charges produced per particle radius for different metal particles with -2 V bias on the middle plate. Using charging model by John (1995).The black dashed lines represent 1 and 2 electron charge limit and the red dot-dashed line represents the electron emission limit.

8.3.2 Particle Density Dependance

Smoke particles in the atmosphere have been theorised to have both 2 and 3 g/cm3 density. More recent papers conclude with a 3 g/cm3 density (Antonsen et al., 2017) and this value has been used for all the charging models. Effect of varying the density is shown in figure 8.7, where there are more charges generated by using a density of 3 g/cm3 and the difference increases with particle size. The difference is less for the unbiased middle plate. This is due the charging model of John (1995) has generated charge being proportional to the potential difference between the particle and the surface while the resulting charge is proportional to $\rho^{2/5}$, resulting in a larger difference for a a higher potential difference. The generated charge of the biased middle plate is however much higher than the electron emission limit. It can be noted that the charging model of Adams and Smith (1971) is proportional to $\rho^{1.1}$ but does not include the potential difference and the model of Wang and John (1988) is approximately proportional to the potential V_c and $\rho^{1/2}$, this is due to the complexity of the equations and the relation is not 1:1. The model by Matsusaka et al. (2010) is proportional to the potential but does not on the density of the particles. This can be seen in table 8.3.

Table 8.2: Comparison of the dependence of each charging model to the density and the potential difference between the particle and the surface

Charging Model	Density	Potential
Adams and Smith (1971)	$\rho^{1.1}$	–
Wang and John (1988)	$\approx \rho^{1/2}$	$\approx V_c$
John (1995)	$\rho^{2/5}$	V_c
Matsusaka et al. (2010)	–	V_c

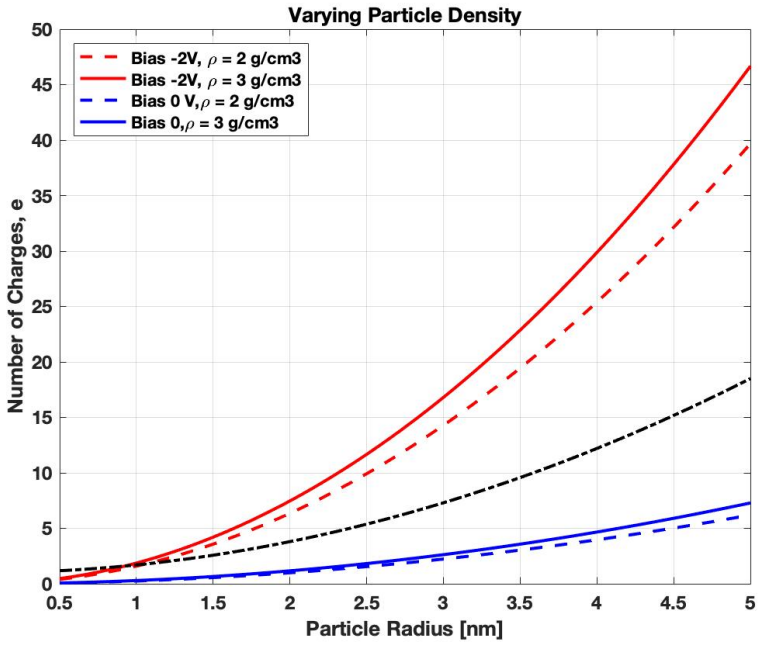

Figure 8.7: Comparison of charge produced per particle size with density of 2 g/cm3 and 3g/cm3 and a -2 V biased middle plate and no bias on the middle plate.The black dot-dashed line is the electron emission limit. The particles are iron particles using the charging model of John (1995)

8.3.3 Separation Distance Dependence

The separation distance is the minimum distance between the particle and the surface and the generated charge decreases for larger values of this distance as is seen in figure 8.8. The number of charges per particle radius is plotted for

several multiples of the Bohr radius. The Bohr radius has been chosen as the minimum distance obtained between a colliding particle and a surface. By varying the distance the minimum size of particles that are able to generate one electron charge increases. The largest distance Z plotted equals a little over 1 nm distance, this result sin particle below 3.5 nm to not be able to generate any charge. The difference between the number of charges for different values of Z also decreases with increasing distance between the particle and the surface. Both the models of John (1995) and Wang and John (1988) depend on the value of Z as does Matsusaka et al. (2010), but the model of Adams and Smith (1971) does not.

Table 8.3: Comparison of the dependence of each charging model to the separation distance, Z, between the particle and the surface

Charging Model	Separation Distance
Adams and Smith (1971)	–
Wang and John (1988)	$\approx 1/Z$
John (1995)	$1/Z$
Matsusaka et al. (2010)	$1/Z$

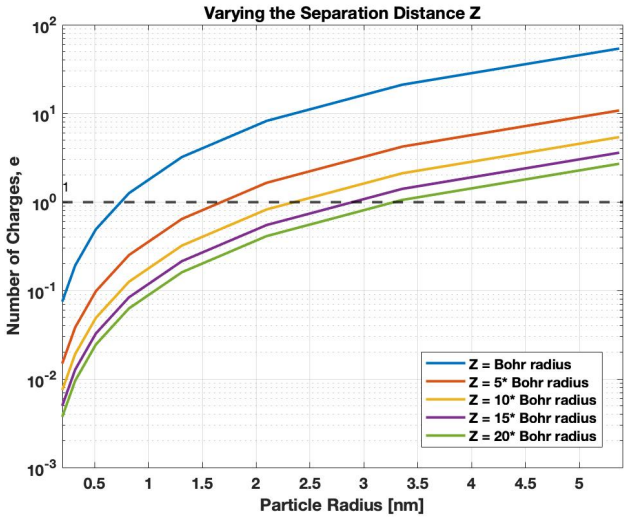

Figure 8.8: Varying the separation distance Z with multiples of the Bohr radius, between the particle and the middle plate. Using the charging model of John (1995) with a biased middle plate of -2V

8.4 Particle Speed Dependance

All the charging models depend on the initial speed of the particles except Matsusaka et al. (2010), with the velocity dependence given in table 8.4. The particles in the probe have been simulated (from airflow simulations) to have around $v = 500m/s$ inside the probe as their initial velocity, and in figure 8.9 this particle velocity is compared to particle velocities of 250, 750 and 1000 m/s. Since the model of John (1995) has the charge proportional to $v^{4/5}$ the resulting charge increases with increasing speed but the increase is more noticeable for the difference between 250 and 500 m/s than for 500 to 750 m/s. The velocity for the model of Adams and Smith (1971) the velocity dependence has been chosen to be squared, their results for iron particles yielded this dependence, while for other metal particle the dependence was different, from the order of 2- 3.3 dependence.

Table 8.4: Comparison of the dependence of each charging model to the incident velocity of the particle to the surface

Charging Model	Velocity
Adams and Smith (1971)	v^2
Wang and John (1988)	$\approx v$
John (1995)	$v^{4/5}$
Matsusaka et al. (2010)	–

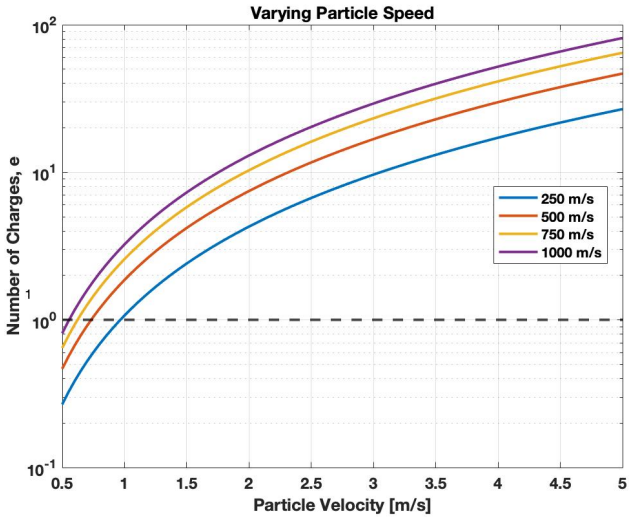

Figure 8.9: Varying the initial impact speed of the particles as they collide with a -2 V biased middle plate. The velocity is varied from 250 to 1000 m/s. Using charging model of John (1995)

8.5 Resulting Current

Using the number density and size distribution from figure 2.3 the total current from each charging model can be calculated for positive, neutral and negative particles. The values given in table 8.5 are used for calculating the current for all charge states of MSPs. For the neutral particles largest current is shown to be from the model of Wang and John (1988) with a maximum value of almost 15 nA, more than enough to be able to be detected on the middle plate. The models by John (1995) and Matsusaka et al. (2010) show as before the same current since it depends on the same number of charges generated per particle size. The current from model Adams and Smith (1971) is at maximum 0.75 nA, this is possible to measure by the middle plate but that would depend on the effective shielding of the ambient ions, since the current generated by the ions would be hard to distinguish from such a small current. The currents calculated for the positive and negative particles are shown in figures 8.11 and 8.12, here it is assumed that all pre-charge on particles is transferred first to the middle plate and then a current is generated by the particle as if it was neutral. The positively charged MSPs in the model have lower number density than the neutral, especially at higher altitudes, with the maximum density being around 65 km. Due to large particles residing in more abundance at lower altitudes the resulting current is largest from 60 to 65 km.

The magnitude is at maximum 10 nA fro the charging model of Wang and John (1988) as for the neutral particles. The negative particles show a rather different result, this is due to the fact that it is assumed that the particles first give away their negative pre-charge and then have the possibility of gaining an electron right after in the impact. This is valid since the pre-charge transfer happens instantly in the collisions Wang and John (1988). The contribution from the pre-charge is dominant for all the models except Wang and John (1988), where the current from the contact charging is higher than the pre-charge transferred resulting in a positive current contribution, while the other models give a negative current contribution. The magnitude of all the models is however not that large and would be hard to discern from the contribution of the positive and neutral particles.

Table 8.5: Parameters used in calculating the current for neutral, positive and negative MSPs for different charging models.

Parameter	Value
Incident Velocity	500 m/s
Density	3 g/cm3
Particle Composition	Iron
Bias on Middle Plate	-2V

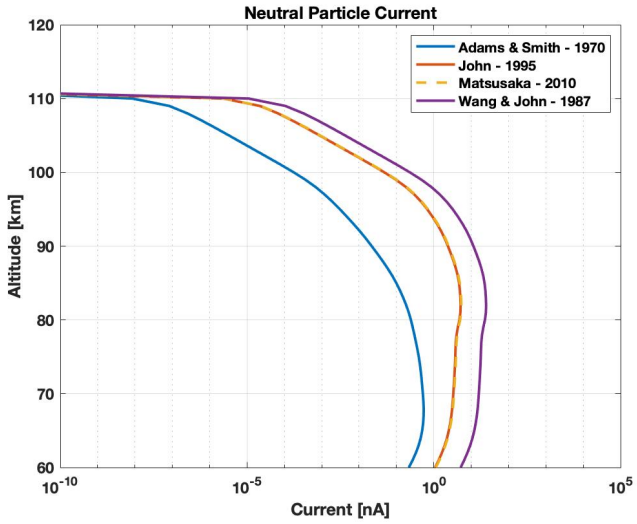

Figure 8.10: Total current for all size distributions for neutral MSP particles with altitude. Using data from model by Baumann et al. (2015) and Megner et al. (2006)

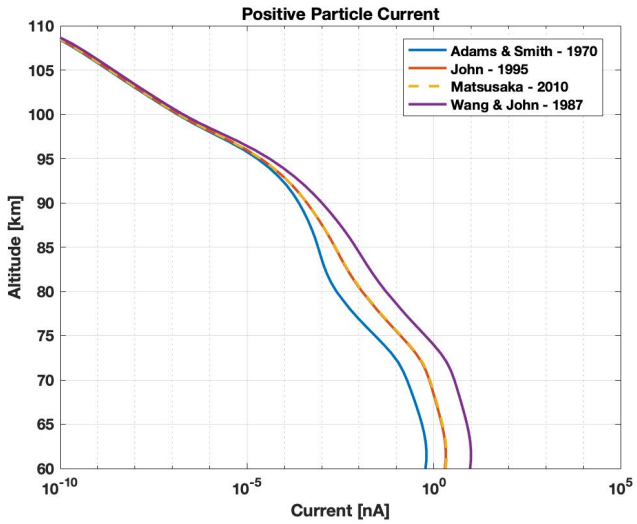

Figure 8.11: Total current for all size distributions for positive MSP particles with altitude. Using data from model by Baumann et al. (2015) and Megner et al. (2006)

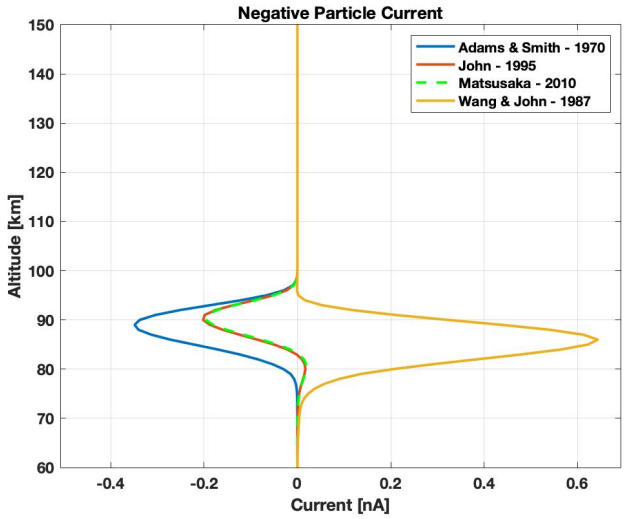

Figure 8.12: Total current for all size distributions for negative MSP particles with altitude. Using data from model by Baumann et al. (2015) and Megner et al. (2006)

Now by comparing the calculated currents above to the measured current from the middle plate in figure 8.13 shows that the altitude distribution of the MSPs from the model are at altitudes where there was no measured current on the middle plate. This can be due to the model used for the altitude distribution being during September and not January like the rocket launch, or that the total current generated by the MSPs is so low that is is smaller than 1 nA and remains hard to discern from the much larger ion contribution at higher altitudes. It is possible that the MSPs are in layers at 50-60 km and at 80 to 90 km, with larger sizes at the lower altitude contribution to the large current measured after the nose-cone separation and the smaller particles contributing somewhat to the lower current at the higher altitudes, but due to the large ion current as has been discussed before it is hard to discern if there is an ion contribution and a very small dust contribution.

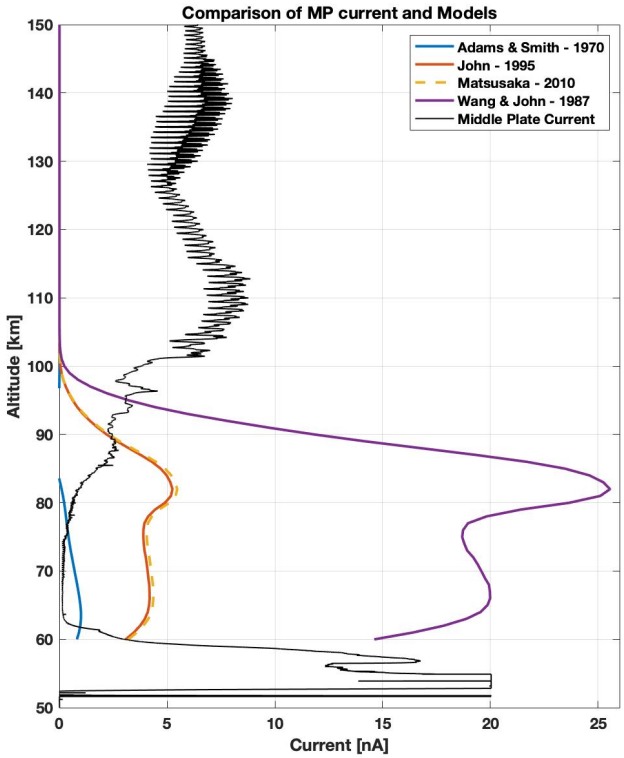

Figure 8.13: Comparison of the measured current from the middle plate to the calculated current from the different charging models due to neutral and positively charged particles.

In figure 8.14 the current calculated from charging model Wang and John (1988) is compared to the measured current from the middle plate. The total current for several size ranges are calculated and plotted. Showing that the relative magnitude of the currents is similar but the altitude distribution is not. This can be due to either the charging model is a large over estimate of the possible generated current or that the main MSP distribution was at a lower altitude than the size model. The current from particle size of 0.2 to 1.3 nm (the yellow line) shows that this magnitude of current is quite comparable to the current measured between 55 and 60 km.

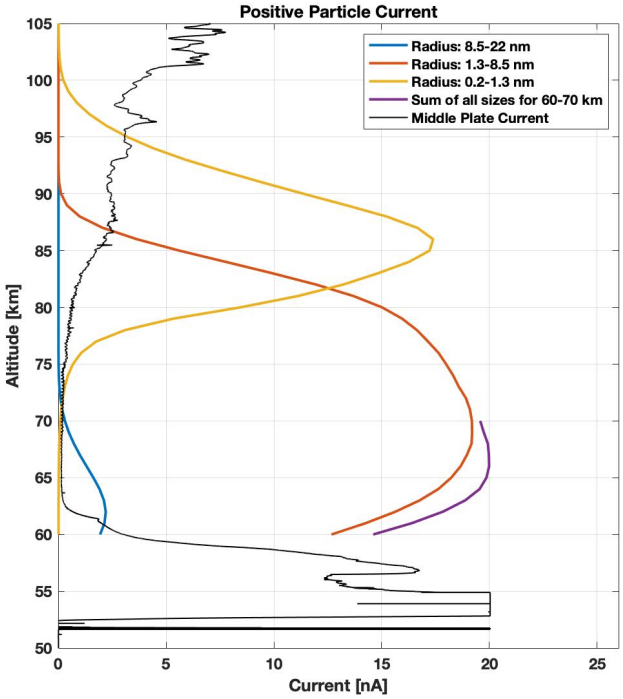

Figure 8.14: Comparison of the measured current from the middle plate to the calculated current from the cahrging model of Wang and John (1988) by varying the particle size

Now by comparing the currents generated on the GB1 grid (biased to -10V) to the currents produced by the charging models for positive and neutral particles. Showing no correlation between the calculated current and the GB1 current, the signal from the GB1 current at altitudes 60 to 80 km remains unexplained thought. This portion of the current could very well be due to positively charged dust particles, however without shielding out the ambient ions and electrons this is very hard to conclude on.

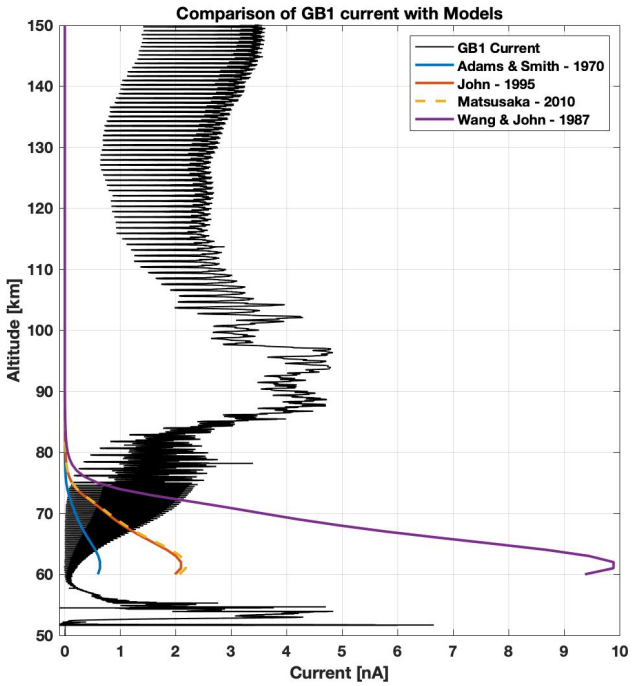

Figure 8.15: Comparison of the measured current from GB1 grid and the charging models due to positive and neutral particles.

Comparison of the measured current from GB2 (positive potential of + 10 V) with the charging models generated current by negative particles shows that the magnitude of the charging model of Wang and John (1988) for altitudes 60 to 80 is not all that different form the measured signal between 60 and 80 km. This would again be better confirmed by running the size distribution model for dust size and altitude distribution for December conditions and solar zenith angle of 95 °. It is also unclear if the negative MSP number density for December conditions would be comparable to the September conditions. If they are comparable then the current is rather adequately explained by the charging model of Wang and John (1988).

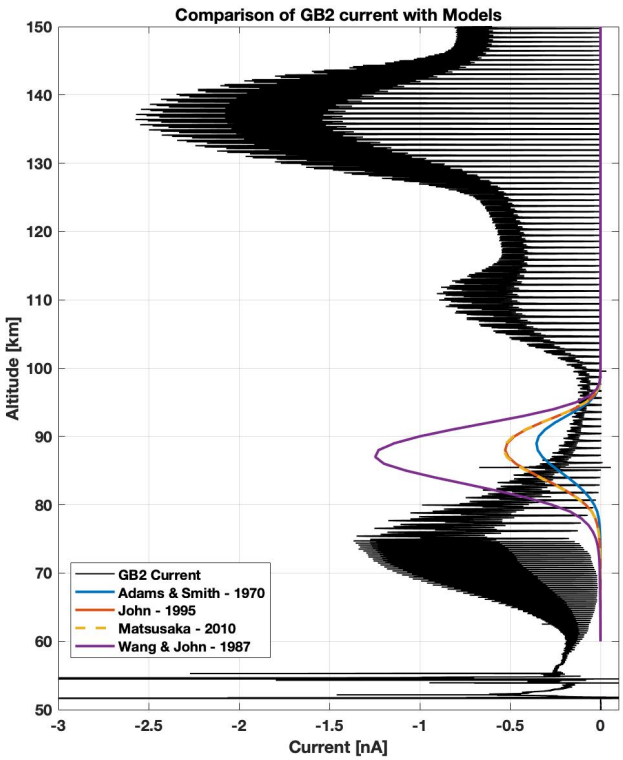

Figure 8.16: Comparison of the measured current from GB2 grid and the charging models due to negative particles.

Chapter 9

Conclusion and Discussion

This thesis has focused on the payload charging by ambient plasma and photocurrent from solar flux, the possible influence of direct sun on the middle plate and two bottom grids of SPID. Several charging models have also been discussed and the effect of variations of their inherent parameters, as well as the comparison of each charging models and the resulting current with the middle plate and grids. The considerations on the charging of the payload showed that the it is dominated by ambient electrons by an order of magnitude larger than the estimated photocurrent and by three orders of magnitude larger than the ion current in the ram direction of the rocket. This is just an estimated electron current since the accurate payload potential was not measured on the rocket and thus can only be estimated. Estimating the photocurrent required lot of data regarding number density and absorption cross section of molecular oxygen and ozone, this induces large uncertainties since there are large variations in the measured absorption cross sections of these constituents that also varied with temperature. Additionally due to the high solar zenith angle of 95 °the atmosphere absorption below 70 km was so high that almost all incident radiation was absorbed. As a result in the absorption of molecular oxygen was the dominating factor for examining the photocurrent on the payload for the the rocket flight. Estimates made by considering the photocurrent on a rotating aluminium cylinder showed at maximum 0.45 mA, which is one order of magnitude smaller than the electron contribution, and since the final resulting current was smaller than the dominant electron current it only slightly contributed to the payload potential being a little less negative than if only the electron current was there.
A more interesting aspect of the calculated photocurrent was looking at the possibility of there being a photoemission contribution on the middle plate and the two bottom grids. This would occur if they were in direct sunlight due to low sun. Estimating the photocurrent on the grids was done with some simplifications, the photoelectric yield for silver is much higher than for stainless steel and aluminium

and creates a very high resulting current, however since the grids area is quite small and the amount they stay in sunlight this was reduced quite a bit. However not enough and the resulting current was several orders of magnitude larger than the grid currents. For the middle plate current however the results shoed that the magnitude of the coning current could very well be due to direct sunlight on the grid. An accurate result of the photocurrent on the grids should however be calculated with ray-tracing analysis and photoemission experiments on the actual grids to determine if the current can indeed be caused by direct sunlight.

Comparison of the middle plate and the two bottom grids with possible ion and electron current derived from EISCAT measurements during the flight showed that there are large correlations between the ion current and the grids that measure positively charged particles. At altitudes of 80 to 110 km there are clear similarities in the measured signal and the ion number density and the signal follows the ion current curve very well. This indicated that the first two grids were not adequately biased to shield out the ions throughout the flight, since they were saturated almost instantly it was impossible to say if this was the case or not by just looking at the signals. Comparison off the grid that measured a negative current the GB2 grid showed no correlation with the electron current at altitudes below 100 km. There are some similarities above this altitude, the general shape increases like the electron current, but the heavy coning motion dominates the general curve too much to be certain of this. Both GB2 and GB1 measure similar negative and positive currents between 60 and 80 km. And since EISCAT is not accurate below this altitude the number density measured is close to zero, whether this part of the signal could be due to small negative and positive dust particles is possible. The measured currents are on the order of 1.5 nA for the negative current and a little over 2 nA for the positive current, however this is unlikely since there is almost no current on the middle plate corresponding to dust at these altitudes. The current from the middle plate seems to be dominated by ions above 80 km, it is impossible to discern if the signal is only due to ions or if there is a small dust component added as well. The large signal measured below 60 km is the most promising one to be due to dust, the nose cone separation is just before that and there is a possibility that the signal can be connected to that, but due to the high speed of the rocket and fast airflow this is however unlikely. This would require a new rocket flight, that would possibly manage to fix the saturation fo the top grids and thus be able to shield out the ambient plasma.

Comparison of different charging models on the charging of the particles on the middle plate shows that some theories indicate that particles below 2 nm cannot generate charge by collision alone. This possibility is improved if the particles slide on the middle plate and thus have more change to generate charge, this is however not so likely since the microscopic surface of the middle plate is most

likely not smooth and would rather cause the particle to disintegrate or rip apart to even smaller radiuses. This effect will need to be studied for future rocket launches. The charging model by Matsusaka et al. (2010) shows more promise for the smaller particle range where 0.5 nm particles are able to generate some charge for spherical iron particles. The theory by Adams and Smith (1971) is very dependent on the particle velocity and density and increases to very high currents with increasing particle size. Comparison of the charging models indicates that there are such large discrepancies that to chose one over the other would be pure guess work, and experiments with SPID and the charging efficiency of the middle plate needs to be examined further to better understand the charging behaviour of such small particles with the probe at these high speeds.

Literature give the maximum charge of nanoparticles below 10 nm to only be singly charged, and particles over that radius can be doubly charged, this fact is however considering particles in the atmosphere being charged by electron and ions and not charging by triboelectric charging in high speed collisions. The maximum charge possible for a nanometer particles has been concluded to be dominated by the electron emission limit, assuming that the smoke is made of rather sturdy metal material. This result in one charge for 0.5 nm particles and an exponentially growing limits for increasing radius. The effect of the bias of -2 V on the middle plate work function is not straight forward. In theory this should increase the work function by 2 V and result in 6.3 eV, if this is the case then that means that there is increased chance of generating charge of the smaller dust particles radiuses. since the generated charge is proportional to the work function difference, the particle velocity and the minimum separation distance. All these factors influence the particle charging. It is also noteworthy that since MSP have been shown to have work function of 4-4.6 eV (Rapp et al., 2012) and the work function of stainless steel is 4.3 eV. And by not biasing the middle plate the current generated would be both negative and positive. This effect needs to be studied in detail with laboratory analysis of dust charging in the probe. By comparing the theory of (Wang and John, 1988) to the currents measured by the middle plate and the two bottom grids shoed that the magnitude of the current was non that far off for negative particles and GB2 grid and the sum of the total current for neutral, positive an negative particles compared to the middle plate. This can be explained by the incorrect altitude distribution of the MSP size and number density. In the future this can be better analysed by running a model for December conditions of the size distribution with altitude.

It is quite difficult to find a good charging model that takes into account the entire collisions, especially for small particles, most models focus on micrometer sized particles and lower impact velocity and large uncertainties rise in extrapolating these models to the particle velocity and size discussed for SPID. Another prob-

lem is the composition for MSPs, where the charge transfer depends largely on the composition and how they interact in collisions, the charging models all assume metallic spherical particles which is most likely not the case for MSPs. As was the findings of Rapp et al. (2012) the particles are assumed to have a hydroxide composition, this makes the particles not purely metal and causes the charge transfer to differ, especially in the collisions and how the particles collide. A benefit would be to study MSP composition possibilities in the lab and test them in high velocity collisions, as well as determine their accurate work function and mechanical properties like the young's modulus and poisson s ratio. As well as varying the composition of the middle plate and examine its microscopic surface. For small particles colliding with rough impure surfaces this causes severe discrepancies, and several authors have concluded that the state of the surface often dominated the charging behaviour of the particles. By doing molecular dynamic simulations of the collisions by taking into account the hight velocity, rough surface, increased density in the probe and added temperature the charging process could be better defined. Launching experiments on rockets is hard, anyone who has can confirm that. Overall in the scheme of things SPID was relatively successful for a first try, many lessons learned and hopefully this will not be the last launch. SPID has promise as a dust detector, for it to be useful there are several thing that need to be improved and tested, but most things that cant be done. Testing the middle plate with impacting nanoparticles is probably the one that would be most hard, but it wouldn't be too bad to test it with larger particles either.

So as a summary: in order for SPID to concretely measure MSPs the ambient plasma needs to be shielded out, the charging process needs to be simulated and experiments done to confirm this, different materials used for the middle plate need to be considered and determination of the MSP possible mechanical constants defined. The charging model by Wang and John (1988) (plastic deformation) seems to be the most promising considering the data.

Bibliography

NG Adams and D Smith. Studies of microparticle impact phenomena leading to the development of a highly sensitive micrometeoroid detector. *Planetary and Space Science*, 19(2):195–204, 1971.

Aksteel. Product Sheet AI ,SI 316L Stainless Steel, Accessed: 2019-05-20. URL `https://www.aksteel.com/sites/default/files/2018-01/316316L201706_2.pdf`.

Tarjei Antonsen, Ove Havnes, and Ingrid Mann. Estimates of the size distribution of meteoric smoke particles from rocket-borne impact probes. *Journal of Geophysical Research: Atmospheres*, 122(22), 2017.

CG Bardeen, OB Toon, EJ Jensen, DR Marsh, and VL Harvey. Numerical simulations of the three-dimensional distribution of meteoric dust in the mesosphere and upper stratosphere. *Journal of Geophysical Research: Atmospheres*, 113 (D17), 2008.

C Baumann, M Rapp, A Kero, and C-F Enell. Meteor smoke influences on the d-region charge balance–review of recent in situ measurements and one-dimensional model results. In *Annales Geophysicae*, volume 31, pages 2049–2062. Copernicus GmbH, 2013.

Carsten Baumann, Markus Rapp, Milla Anttila, Antti Kero, and Pekka T Verronen. Effects of meteoric smoke particles on the d region ion chemistry. *Journal of Geophysical Research: Space Physics*, 120(12):10–823, 2015.

GE Bodeker, Birgit Hassler, Paul Young, and Robert W Portmann. A vertically resolved, global, gap-free ozone database for assessing or constraining global climate model simulations. *Earth System Science Data*, 5(1):31–43, 2013.

Asgeir Brekke. *Physics of the upper polar atmosphere*. Springer Science & Business Media, 2012.

CCMC. Community Coordinated Modeling Center: Nrlmsise-00 atmosphere model, Accessed: 2019-05-28. URL https://ccmc.gsfc.nasa.gov/modelweb/models/nrlmsise00.php.

Diako Darian, Sigvald Marholm, Joakim John Paul Paulsson, Y Miyake, H Usui, Mikael Mortensen, and Wojciech Jacek Miloch. Numerical simulations of a sounding rocket in ionospheric plasma: Effects of magnetic field on the wake formation and rocket potential. *Journal of Geophysical Research: Space Physics*, 122(9):9603–9621, 2017.

Gabriel Giono, Boris Strelnikov, Heiner Asmus, Tristan Staszak, Nickolay Ivchenko, and Franz-Josef Lübken. Photocurrent modelling and experimental confirmation for meteoric smoke particle detectors on board atmospheric sounding rockets. *Atmospheric Measurement Techniques*, 11(9):5299–5314, 2018.

WR Harper. The volta effect as a cause of static electrification. *Proceedings of the Royal Society of London. Series A. Mathematical and Physical Sciences*, 205 (1080):83–103, 1951.

O Havnes, Jörg Gumbel, T Antonsen, Jonas Hedin, and C La Hoz. On the size distribution of collision fragments of nlc dust particles and their relevance to meteoric smoke particles. *Journal of Atmospheric and Solar-Terrestrial Physics*, 118:190–198, 2014.

Ove Havnes, J Troim, T Blix, W Mortensen, LI Naesheim, E Thrane, and T Tonnesen. First detection of charged dust particles in the earth's mesosphere. *Journal of Geophysical Research: Space Physics*, 101(A5):10839–10847, 1996.

Mark E Hervig, James SA Brooke, Wuhu Feng, Charles G Bardeen, and John Plane. Constraints on meteoric smoke composition and meteoric influx using sofie observations with models. *Journal of Geophysical Research: Atmospheres*, 122(24), 2017.

HE Hinteregger. Representations of solar euv fluxes for aeronomical applications. *Advances in Space Research*, 1(12):39–52, 1981.

Donald M Hunten, Richard P Turco, and Owen B Toon. Smoke and dust particles of meteoric origin in the mesosphere and stratosphere. *Journal of the Atmospheric Sciences*, 37(6):1342–1357, 1980.

ASM Aerospace Specification Metals Inc. Stainless Steel 316L: Material properties, Accessed: 2019-04-01. URL http://asm.matweb.com/search/SpecificMaterial.asp?bassnum=MQ316P.

Walter John. Particle-surface interactions: charge transfer, energy loss, resuspension, and deagglomeration. *Aerosol science and technology*, 23(1):2–24, 1995.

Judith Lean. The sun's variable radiation and its relevance for earth. *Annual Review of Astronomy and Astrophysics*, 35(1):33–67, 1997.

Ingrid Mann, Nicole Meyer-Vernet, and Andrzej Czechowski. Dust in the planetary system: Dust interactions in space plasmas of the solar system. *Physics reports*, 536(1):1–39, 2014.

Shuji Matsusaka, Hiroaki Umemoto, Matami Nishitani, and Hiroaki Masuda. Electrostatic charge distribution of particles in gas–solids pipe flow. *Journal of Electrostatics*, 55(1):81–96, 2002.

Shuji Matsusaka, H Maruyama, T Matsuyama, and M Ghadiri. Triboelectric charging of powders: A review. *Chemical Engineering Science*, 65(22):5781–5807, 2010.

Linda Megner, M Rapp, and J Gumbel. Distribution of meteoric smoke–sensitivity to microphysical properties and atmospheric conditions. *Atmospheric Chemistry and Physics*, 6(12):4415–4426, 2006.

NREL. U.S. Department of Energy : Air mass zero: Extraterrestrial solar irradiance spectra, Accessed: 2019-05-22. URL `https://www.nrel.gov/grid/solar-resource/spectra.html`.

University of Colorado Boulder. Laboratory for Atmospheric and Space Physics - University of Colorado Boulder: Sorce - solar spectral irradiance data, Accessed: 2019-04-01. URL `http://lasp.colorado.edu/home/sorce/data/ssi-data/`.

John MC Plane, Wuhu Feng, and Erin CM Dawkins. The mesosphere and metals: Chemistry and changes. *Chemical reviews*, 115(10):4497–4541, 2015.

Markus Rapp, JMC Plane, B Strelnikov, G Stober, S Ernst, Jonas Hedin, Martin Friedrich, and U-P Hoppe. In situ observations of meteor smoke particles (msp) during the geminids 2010: constraints on msp size, work function and composition. In *Annales geophysicae*, volume 30, pages 1661–1673. Copernicus GmbH, 2012.

NH Rees. *Physics and chemistry of the upper atmosphere*, volume 1. Cambridge University Press, 1989.

S Rennecke and AP Weber. Charge transfer to metal nanoparticles bouncing from conductive surfaces. *Aerosol Science and Technology*, 48(10):1059–1069, 2014.

RG Roble and BA Emery. On the global mean temperature of the thermosphere. *Planetary and Space Science*, 31(6):597–614, 1983.

Chetan Singh Solanki. *Solar Photovoltaics: fundamentals, technologies and applications*. PHI Learning Pvt. Ltd., 2015.

The Engineering ToolBox. Youngs Modulus for common materials, Accessed: 2017-12-1. URL `https://www.engineeringtoolbox.com/young-modulus-d_417.html`.

Hwa-Chi Wang and Walter John. Dynamic contact charge transfer considering plastic deformation. *Journal of aerosol science*, 19(4):399–411, 1988.